

PASSIVE MAGLEV: AN INVESTIGATION ON DIAMAGNETIC LEVITATION OF GRAPHITE SHEETS

Jethro Chai Tsin Kai¹, Kevin Goh Ke Ming², Chloe Soh Enqi³, Wee Wei Hsiung⁴

¹Hwa Chong Institution, 661 Bukit Timah Rd, Singapore 269734

²NUS High School of Mathematics and Science, 20 Clementi Ave 1, Singapore 129957

³Raffles Institution, 1 Raffles Institution Lane, Singapore 575954

⁴DSO National Laboratories, 12 Science Park Drive, Singapore 118225

1. ABSTRACT

Graphite is a strongly diamagnetic material, and thin sheets of graphite can levitate stably above a 2x2 array of cubic permanent magnets with alternate poles facing upward. Two forms of graphite, pyrolytic graphite and isostatic graphite, are observed to have different orientation in stable levitation. We hypothesize that this is due to anisotropy of pyrolytic graphite and show that it is using an analytical model. We also go on to investigate the resonant behaviour, equilibrium position and temperature dependence of pyrolytic and isotropic graphite sheets of various sizes levitating in an array of permanent magnets, making use of novel and accessible methods without the need for advanced equipment. Using these results, we characterize the magnetic susceptibility at room temperature experimentally as well as the change in susceptibility with different temperatures. We conclude that increasing temperature leads to reduced magnitude of diamagnetic susceptibility, increasing sheet size leads to decreased frequency of each mode of oscillation for both types of graphite, and the tilting and vertical modes of pyrolytic and isostatic graphite sheets have very similar frequency experimentally.

2. INTRODUCTION

While theorised to be mathematically impossible by Earnshaw [1], stable and passive magnetic levitation is in fact, possible due to the existence of materials with negative susceptibility ($\chi < 0$). This phenomenon is also known as diamagnetic levitation. When a magnetic field is applied to diamagnetic materials, a magnetic field in the opposite direction is induced, causing the material to experience repulsive force, and hence granting it the ability to levitate stably in a magnetic field. Its passivity allows for potential applications in sensing due to its low complexity, energy costs, and advantages of physical isolation provided by the levitation.

Our main objective is to analyse the behaviour of a graphite sheet levitating above an array of 2×2 magnets with alternating poles pointing up of pyrolytic graphite and isostatic graphite.

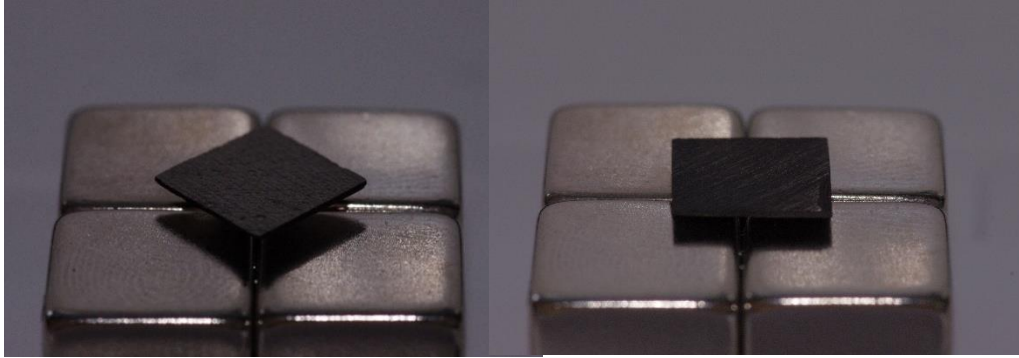


Figure 1. Image of levitating graphite plates. Figure on the left is the pyrolytic (anisotropic) graphite sheet, levitating with $\theta_z = \frac{\pi}{4}$. Figure on the right is the isotactic (isotropic) graphite sheet, levitating with $\theta_z = 0$.

Preliminary observations show that the pyrolytic graphite behave differently from isotactic graphite, such as its equilibrium twist angle, despite both experiencing the same magnetic field. We hence hypothesise that these difference in behaviour arises from the anisotropy of the pyrolytic graphite, compared to the isotropy of the isostatic graphite, which led to a difference in magnetic energy density for the sheets. We hence set out to analyse the behaviours of both sheets, such as their equilibrium position, but also oscillatory modes, frequencies theoretically but formulating a governing equation, as well as experimentally. To better understand the behaviour of the graphite sheets in different conditions, we also experimented with different lengths of each graphite sheet, as well as the change in force with respect to levitation heights. Furthermore, to better characterise their behaviour, we also experimentally derived the trend between the temperature of the sheet and its susceptibility.

MATERIALS AND METHODS

1.1 Theoretical formulations

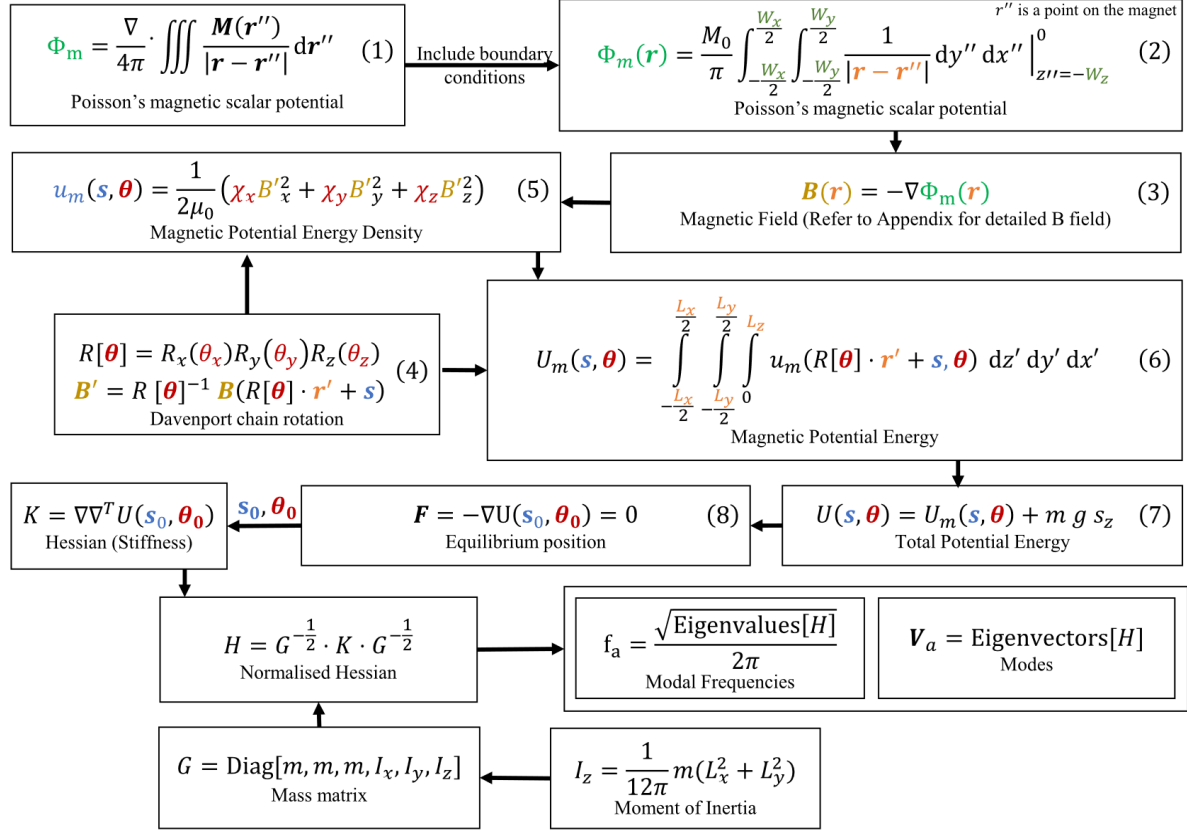


Figure 2. Flowchart of equations used in theory model

To obtain the governing equations for the system, the gradient of magnetic equivalent of Poisson's equation is used to define the magnetic potential energy density, which is then integrated across the graphite sheet to obtain its magnetic potential energy. Fully analytical equations describing the magnetic field (Appendix A) around the magnetic array were derived and then used to calculate the magnetic potential energy and subsequently the equilibrium positions of the graphite sheet and oscillation frequencies and modes. Detailed derivation can be found in Appendix B.

1.2 Materials

5 sheets of $50 \times 40 \times 3 \text{ mm}$ of isostatic pressed graphite sheets were obtained from Lixada mall on Lazada. $10 \times 10 \times 0.35 \text{ mm}$ and $5.3 \times 5.2 \times 0.35 \text{ mm}$ pyrolytic graphite sheets were obtained from Dr Chen Xianfeng (A*STAR). $10 \times 10 \times 10 \text{ mm}$ N50 Neodymium magnets with NiCuNi plating were obtained from SG Magnetics. $30 \times 30 \times 4 \text{ mm}$ magnets with NiCuNi plating were obtained from Supreme Magnets[®]. A FLUKE Ti450 digital thermal imager, which had an error of $\pm 2^\circ\text{C}$ [2] was used to track the temperature of the graphite during heating experiments. A high-power torchlight was used to heat the graphite sheet during levitation experiments to determine susceptibility change with temperature. Wolfram Mathematica and Octave GUI were used to visualise our mathematical models. The cameras used for these experiments are a Samsung SM-N986B (main camera) for video and a Pentax K5-II with DFA 100mm F2.8 Macro (WR) for static height measurements and all other photos.

1.3 Characterization of neodymium magnets

To characterize the magnets used, magnetic field strength from a singular cube magnet was measured with a Gauss meter with varying distance between the probe and the magnet. The magnetization was then fit using equation (3) to the magnetic field strengths measured. Magnetisation was determined to be 1.314 T. Fit can be found in Appendix C.

1.4 Preliminary characterization and preparation of graphite sheets

Pyrolytic graphite and isostatic graphite sheets were shaped using a pen knife and thickness was controlled using sandpaper of grits 80-, 200-, 400-, 1200-. The lengths L_x, L_y of each graphite sheet were then measured using digital vernier callipers, which was also used to ensure even thickness across the sheet. Their thickness L_z was measured using a micrometre screw gauge. The mass m of the sheets were then measured with a 4 d.p. (in grams) electronic weighing scale. Resistivity was determined using the Van der Pauw method [3].

1.5 Experimental Setup

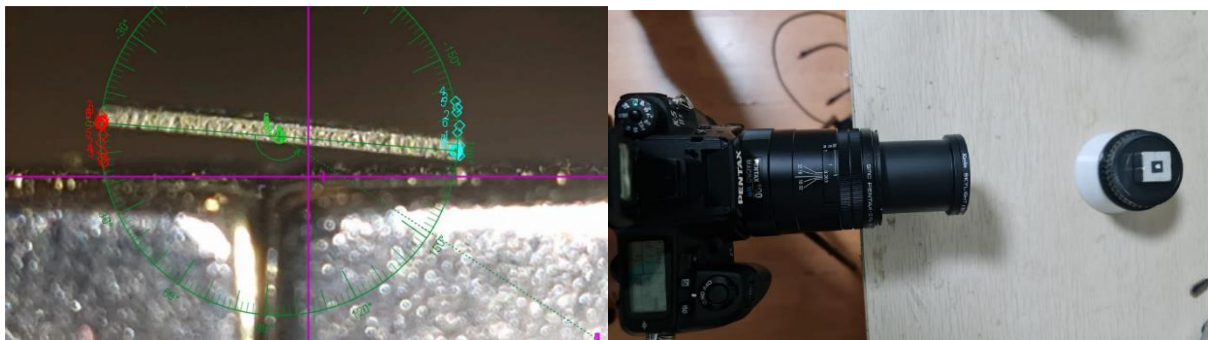


Figure . (Left) tracking tilting motion in tracker. (Right) experimental setup to determine levitation force to height

A 2×2 array of the 10 mm cube magnets with alternating North-South poles facing up was created. Non-magnetic tweezers were used to place the graphite plates in the centre where they levitate.

1.6 Change in levitation height with levitation force

To determine magnetic susceptibility, the levitation height s_z of each of the sheets was measured by taking a picture of the side view of the setup using a camera and converting the pixels between the bottom of the sheet and the magnets to meters. The width of the graphite sheet is used as a reference point for focus and calibration. Magnetic susceptibility was then numerically fit. However, to improve reliability, plastic weights of known mass were added onto the graphite sheet, with the subsequent levitation heights s_z and total weight W were recorded similarly. The net vertical force was then computed for each case using equation (8) and its gradient descent minimized using simulated annealing with a, b-axis susceptibility (χ_x, χ_y) and c-axis susceptibility (χ_z) as parameters.

1.7 Change in levitation height with temperature

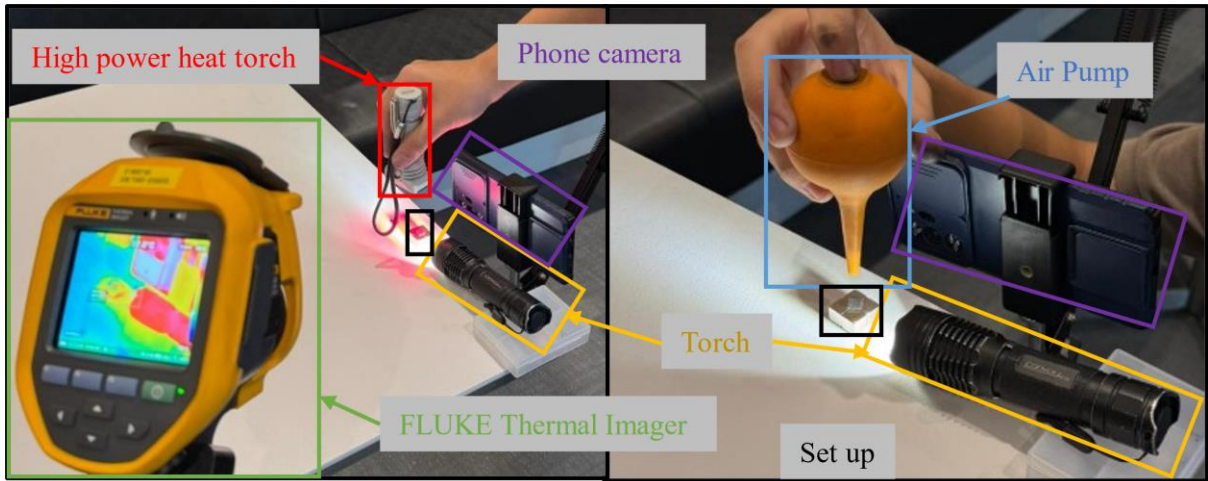


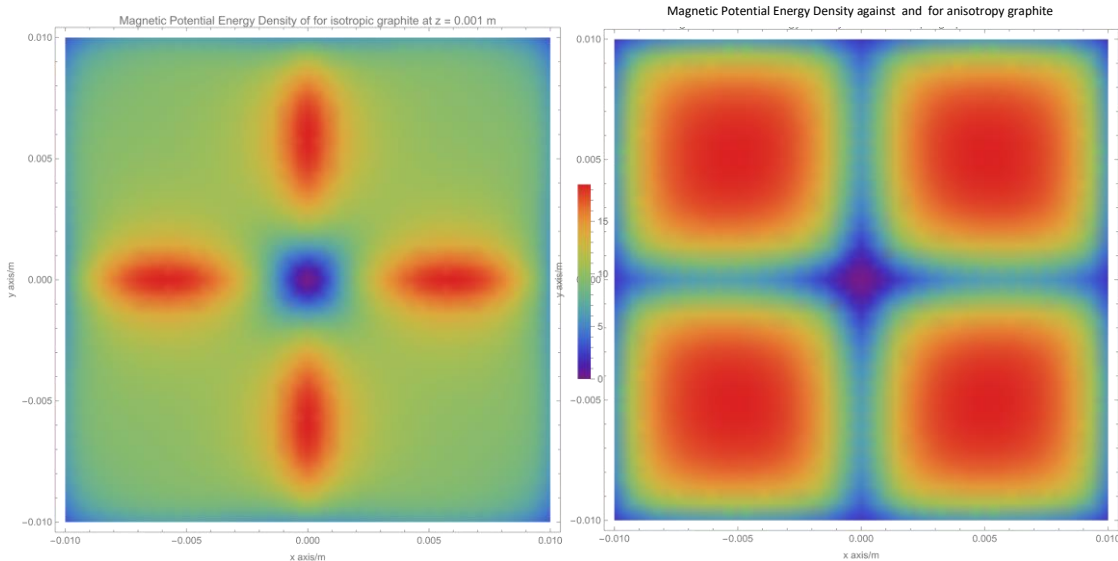
Figure . (Left) Experimental setup to track levitation height against temperature change. (Right) Experimental setup to track tilting and vertical oscillations.

The 7.5 mm isostatic graphite sheet was levitated above the magnetic array and heated with a high-power torch. The temperature of graphite sheet was quantified and recorded down using a thermal imager. The phone camera recording was used to track the motion of the sheet as it cooled.

1.8 Motion of graphite sheet after displacement

The levitating graphite sheet was displaced arbitrarily, and its side view and top view motion was recorded separately with a phone camera. Its centre was then tracked after the oscillation stabilizes. The motion in the different degrees of freedom was then Fast Fourier Transformed (FFT) to determine frequencies.

RESULTS AND DISCUSSION



2.1 Equilibrium position of the graphite sheets



The equilibrium orientation for the isostatic graphite and pyrolytic graphite differs due to the anisotropy of diamagnetic susceptibility in pyrolytic graphite. Since χ_z is higher than $\chi_{x,y}$ for pyrolytic graphite ($\frac{\chi_z}{\chi_{x,y}} > 5$), it is more strongly in the regions directly above the faces of the magnets where B_z is higher, and less strongly repelled by the regions between the magnets where $B_{x,y}$ is higher, even though $|B|$ is higher there. This can be visualized from the magnetic potential energy density plots, where the energy wells are sharply diagonal to the cube magnets for the anisotropic case (Fig 5. (top right)).

In the case of isostatic compressed graphite, diamagnetic susceptibility is isotropic, hence equation (5) simplifies to only $u_m = \frac{1}{2\mu_0} \chi_{x,y,z} |B|^2$, and the individual B field components do not matter. Hence, the sheet avoids regions with higher $|B|$, as this would lead directly to higher magnetic potential energy density, which happen to be at the regions above the intersections between magnets (Fig 5 (top left)). This is more clearly seen in Fig 12 of Appendix E, where

we can see that the magnetic potential energy is minimum when $\theta_z = \frac{\pi}{4}$ for the anisotropic graphite, and $\theta_z = 0$ for the isotropic graphite. Hence, the graphite would orientate itself as shown in Fig 5 (bottom left for isotropic and bottom right for anisotropic).

For example, for a 7.5 mm long graphite sheet, the equilibrium position was mathematically determined to change from $\theta_z = 0$ to $\theta_z = \frac{\pi}{4}$ at $\frac{\chi_z}{\chi_{x,y}} > 1.203$.

2.2 Change in Levitation height with levitation force

As can be seen from Fig 9. of Appendix F, levitation force is higher as levitation height decreases, due to the increase in magnetic field strength closer to the magnet, leading to stronger repulsion. The susceptibility values attained from the fit: $\chi_{x,y} = -6.92 \times 10^{-5}$, $\chi_z = -4.11 \times 10^{-4}$ are within acceptable ranges provided by literature for this specific pyrolytic graphite we procured [4]. This is also the case for isotropic graphite: $\chi_{x,y,z} = -1.379 \times 10^{-4}$.

However, significant deviation can also be observed. This could be explained by the unevenness in the surfaces of the pyrolytic graphite which we were unable to smoothen due to its strong crystalline structure, as well as difference in magnetisation across the magnets led to uneven levitation of the pyrolytic graphite. This was further enhanced by the imprecision of equipment used to determine the levitation height such as the lack of focus around the edges of the graphite sheet. Moreover, larger increments in masses were needed to obtain observable changes in levitation height, leading to limited data points for the gradient descent. Hence, the fitted $\chi_{x,y}$ and χ_z may not be the most accurate one, accounting for the deviations.

2.3 Resonant modes and frequencies

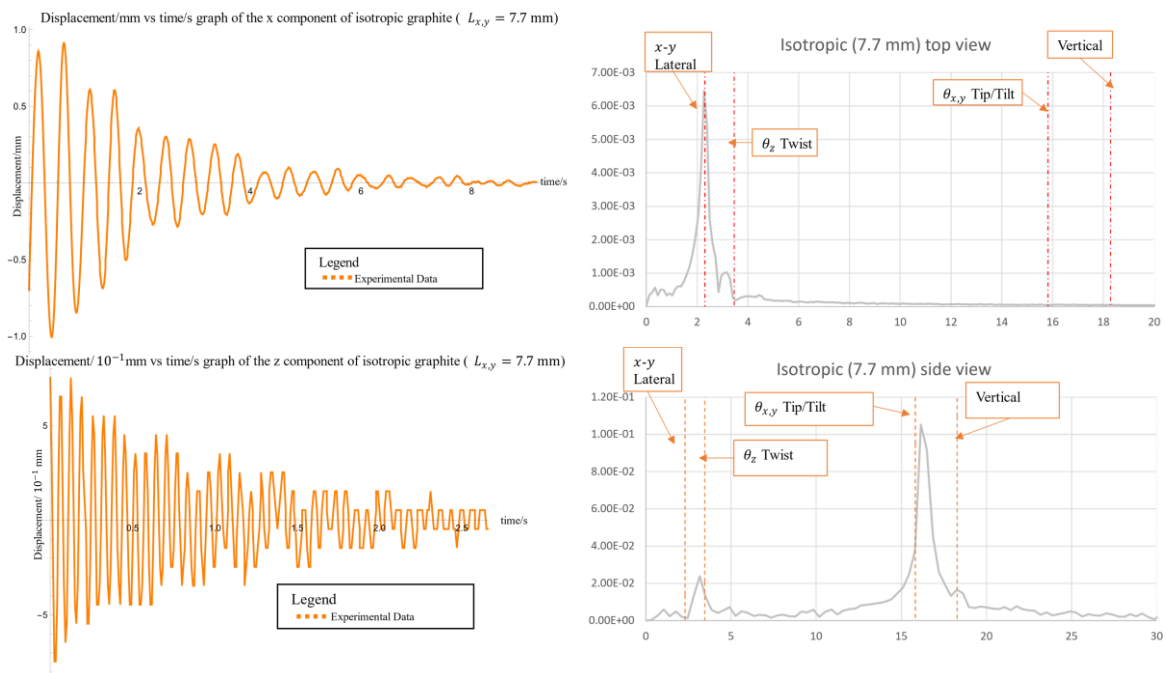
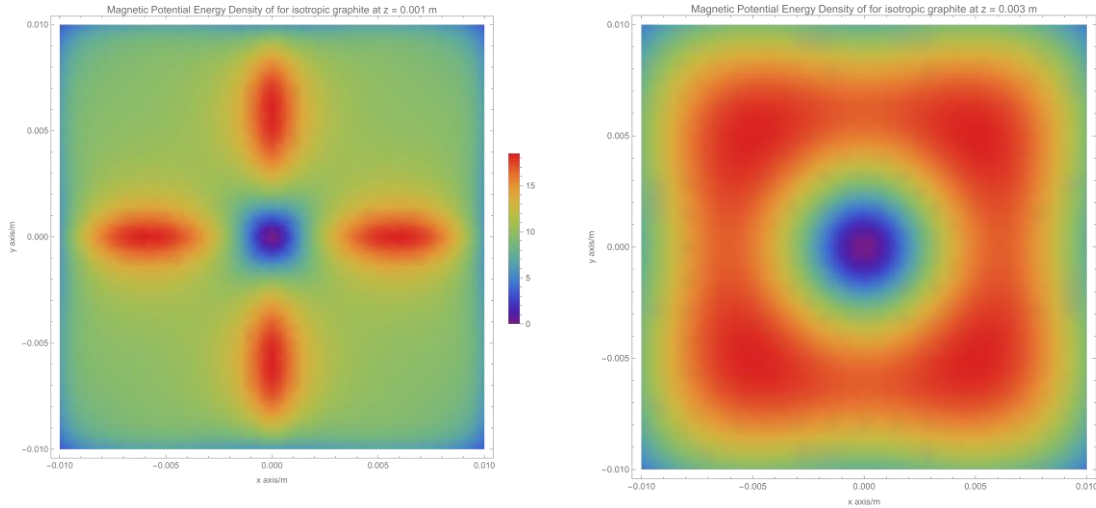


Figure 6. (Top Left) Example of displacement vs time graph obtained from tracker for x component. (Top Right) FFT analysis of data from left, with theoretical frequency peaks marked in orange. (Bottom Left) Example of displacement vs time graph obtained from tracker for z component. (Bottom Right) FFT analysis of data from left, with theoretical frequency peaks marked in orange. Both are for the isotropic graphite at $L_{x,y} = 7.7$ mm

From the FFT graphs (Fig. 14-20, Appendix G), the predominant trend is two peaks at higher frequencies (16.3 Hz, 18.4 Hz) is visible in the side view but disappears in the top view. These peaks should correspond to the tip/tilt vertical modes, since the Eigenvectors (Appendix F) of these two modes have either no (for vertical) or very low (for tip/tilt) lateral components. From the eigenvectors, we also infer that highest frequency (18.4 Hz) corresponds to the vertical mode, and the second highest, to the tip/tilt mode (16.3 Hz). There are two smaller peaks (2.2 Hz, 3.4 Hz). The peak that is visible in both views is most likely the x-y lateral mode, since it also has a vertical component, whereas the twist does not and is most likely the other peak. Due to the amplitude of the lateral oscillation being greater, it is more visible even in FFT of the z component, leading to its peak being quite prominent. Furthermore, the coupling between the modes can be more visibly seen in the displacement-time graph for the z axis because of how small the displacements are compared to the amplitudes of the lateral mode. The x component displacement-time graph, however, seems much cleaner as only two modes are visible, and they are both uncoupled with one another (Appendix F).



Generally, the observed frequencies derived through FFT correlate very closely with the expected values from theory, particularly for the isotropic case. Both theory and experimental results show both twist and tilt oscillation frequency decrease with increasing sheet size that is roughly linear (Fig. 33). However, upon further theoretical investigation, we find that the decrease in frequencies plateaus with increasing length (Fig 27,28). This behaviour corresponds to how the change in levitation height also decreases at a decreasing rate, similar with the change in frequencies. Comparing 7.1 and 7.2, we see that the variation in magnetic potential energy greatly decreases at higher levitation heights, hence leading to a decrease in stiffness value (since the increasing mass and moment of inertia would negate the increase in magnetic potential energy that the sheets with higher lengths receive). Hence, frequency would decrease. Past a certain length, magnetic potential energy starts to decrease with increasing x or y , which leads to the levitation height decreasing with increasing length. Since total magnetic potential energy also decreases, and mass and moment of inertia continues to increase, stiffness decreases. Hence, even in the phase where levitation height decreases with increasing length, frequency decreases. However, this trend could not be captured experimentally due to the low data range and small deviations in mass and thickness.

However, as could be seen from the Fig 22 as well as the FFT graphs in Appendix G, the theory does not match well for the frequencies of pyrolytic (anisotropic) graphite. This could be due to inaccuracies in the susceptibility values fitted using the levitation force to height experiment as described in section 2.2.

2.4 Effect of Temperature

Based on established literature, the magnitude of diamagnetic susceptibility of pyrolytic graphite decreases with increasing temperature, which would lead to decreasing levitation height.

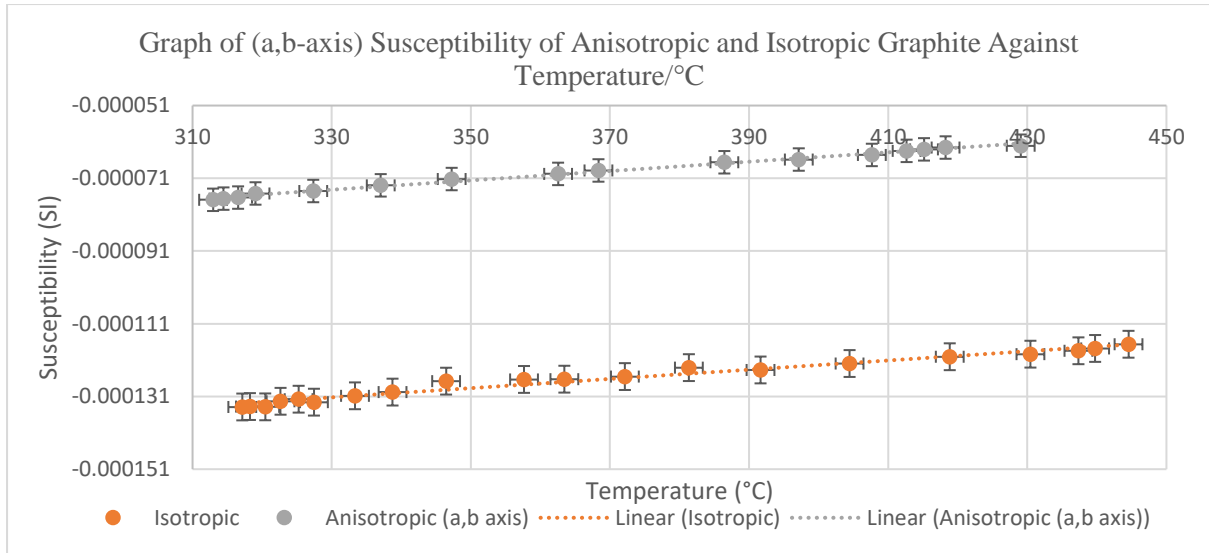


Figure 8. Graph of susceptibility of anisotropic and isotropic graphite against temperature.

From the graph, we can see a clear linear relation between susceptibility and temperature, where increasing temperature leads to lower diamagnetism. This agrees with theoretical estimations [5]. A large component of the susceptibility arises from the contribution from paired core electrons and electrons in the valence band [6]. The electrons in fully filled orbitals have opposite spins, hence the magnetic field from the electrons' spin cancels out, and they do not align themselves with the magnetic field. When a magnetic field is applied, the motion of the electrons alters to create an opposing magnetic field in accordance with Lenz's law [7]. As the conduction band and valence band in graphite touch each other at certain points [7], as temperature rises, electrons transition from the valence band to the conduction band, where they are not bound to orbitals and hence contribute less to diamagnetism [8]. This results in a net decrease in observed susceptibility with temperature. The contribution from the core electrons is independent of temperature since they are too tightly bound to jump into the conduction band, hence at low temperatures, diamagnetism would be less temperature dependent [5]. However, due to logistical limitations, we are unable to investigate the diamagnetism at such low temperatures.

CONCLUSION

In conclusion, we have explored the resonant behaviour of isotropic graphite and pyrolytic graphite sheets levitating in a permanent magnetic trap. Initially, we explained the differing orientation of pyrolytic and isotropic graphite during stable levitation using magnetic field and magnetic potential plots obtained from our analytical model. Using FFTs, we characterize various modes of oscillation of different sizes of graphite plates and compare them to analytical theory values. Using weights to plot levitation force to levitation height for different sizes of sheet, we characterized the diamagnetic susceptibility of both types of graphite. By tracking levitation height change as heated graphite sheets cool to room temperature, we measure the change in magnetic susceptibility with temperature. Finally, we compare the changes in each mode of oscillation among the two types of graphite and differing sheet sizes, finding that tilting modes correspond well between both types of graphite, and larger sheet size leads to decreased oscillation frequency, approaching a linear relationship as sheet sizes approach the maximum size allowing stable levitation. Moreover, we demonstrate the use of accessible tools like a mobile phone camera and the Physlets Tracker app to track small scale oscillations and

movement (on the scale of 0.1-1.0mm) and show that a reasonable level of precision and accuracy can be achieved, especially after processing the oscillation data with FFT analysis.

In the future, we commit to studying theoretically the damping forces, as well as the incorporation of other geometries and larger arrays to better understand its movement in different magnetic fields. The stiffness and other properties of a diamagnetic spring configured with alternating magnet and graphite sheets also present themselves as possible areas of future investigation. To further understand the effect of temperature on its motion, we plan to study the rotational and translational motion of the graphite when a localized spot on the graphite is heated.

Challenges Faced and Lessons Learned

We faced numerous challenges while conducting this research, mainly to do with lack of access to equipment, but we were able to improvise and use highly accessible means to conduct a lot of our experiments.

We originally planned to displace the graphite sheet using amplified voltage signal applied to the magnets causing electrostatic attraction, and a confocal distance sensor or interferometer to graph the vertical displacement. However, without access to either a high power amplifier or an interferometer, we improvised and used a phone camera to record video, and the physlets Tracker app to track vertical displacement, which generated surprisingly accurate displacement-time graphs which were then analysed with FFT analysis. We found that a slight angle in the camera would cause absolute levitation height to be inaccurate, so a tripod and a level app on the phone was used to ensure it is completely vertical or horizontal before recordings are taken. In addition, we applied strong lighting to the setup to minimize digital noise in video files so that they can be tracked more accurately.

For the heating experiments, as we were unable to obtain a high power laser to heat the graphite sheet, we instead used a high power flashlight, and tracked the vertical displacement, again with the tracker app and a phone camera, and temperature with a thermal imager, as the sheet cooled down. Hence the method of heating is irrelevant as it is only cooling down while the motion is being tracked, and we were able to use a regular high power led flashlight to perform heating even though its output dips over time.

When using any kind of camera to track vertical displacement, however, parts of the image are always out of focus due to narrow depth of field at close distances. To mitigate this, we set the focus to be on the thickness of the graphite sheet and took all of our reference points along that plane at the same distance from the camera. This also mitigates parallax error.

Overall, we learned how to make the best out of the equipment and data that we have.

Acknowledgements

We would like to thank our mentor, Dr Wee Wei Hsiung (DSO) who supported us throughout our Research@YDSP journey and teaching us how to do the theoretical analysis, as well as Mr Leslie Lam (DSO), and the EG Division team at DSO, for their help and guidance throughout our internship. Additionally, we would like to thank Ms Sim Yu Jin Emeline (DSO) from the HR team and the rest of the HR team for their aid in the administrative part of this project, as well as DSO National Laboratories for providing us with the opportunity to participate in Research@YDSP 2024. Lastly, we would like to extend special thanks to Dr Xianfeng Chen (A*STAR) for providing us with pyrolytic graphite samples.

REFERENCES

- [1] Earnshaw, S. (1848). On the Nature of the Molecular Forces which Regulate the Constitution of the Luminiferous Ether. *On The Nature of the Molecular Forces Which Regulate the Constitution of the Luminiferous Ether*, 7, 97. <https://ui.adsabs.harvard.edu/abs/1848TCaPS...7...97E/abstract>
- [2] Fluke, “Fluke Ti450 Infrared Camera | Fluke,” *Fluke.com*, Apr. 05, 2022. https://www.fluke.com/en-us/product/thermal-cameras/ti450?srsId=AfmBOop1qrsIEqY1TjELvAFNOohD4OtrPB75WEMgH7n_81ATQil5ndc2.
- [3] Katharina. (2024, December 11). *Van-der-Pauw measurement - Linseis*. Linseis. <https://www.linseis.com/en/methods/van-der-pauw-measurement/>
- [4] Tian, S., Jadeja, K., Kim, D., Hodges, A., Hermosa, G. C., Cusicanqui, C., Lecamwasam, R., Downes, J. E., & Twamley, J. (2024). Feedback cooling of an insulating high-Q diamagnetically levitated plate. *Applied Physics Letters*, 124(12). <https://doi.org/10.1063/5.0189219>
- [5] Banerjee, D., & Bhattacharya, R. (1990). Temperature variation of diamagnetic susceptibility of graphite. In Indian Association for the Cultivation of Science, *Indian J. Phys.* (Vol. 64, Issue 4, pp. 316–320). <https://core.ac.uk/download/pdf/156953823.pdf>
- [6] Adams, E. N. (1953). Magnetic susceptibility of a diamagnetic electron Gas—The role of small effective electron mass. *Physical Review*, 89(3), 633–648. <https://doi.org/10.1103/physrev.89.633>
- [7] Peres, N. M. R., & Castro, E. V. (2007). Algebraic solution of a graphene layer in transverse electric and perpendicular magnetic fields. *Journal of Physics Condensed Matter*, 19(40), 406231. <https://doi.org/10.1088/0953-8984/19/40/406231>
- [8] *Magnetic susceptibility*. (n.d.). Questions and Answers in MRI. <https://mriquestions.com/causes-of-susceptibility.html>

APPENDIX

Appendix A1: Analytical magnetic field expression

$$B_x = -\frac{\delta\Phi_m}{\delta x} = -\frac{M_0}{4\pi} \left(\frac{y-y''}{\sqrt{(x+x'')^2+(y+y'')^2+(z+z'')^2}} \right) \Big|_{x''=-\frac{W_x}{2}}^{\frac{W_x}{2}} \Big|_{y''=-\frac{W_y}{2}}^{\frac{W_y}{2}} \Big|_{z''=-W_z}^0 \quad \#(3.1)$$

$$B_y = -\frac{\delta\Phi_m}{\delta y} = -\frac{M_0}{4\pi} \left(\frac{x-x''}{\sqrt{(x+x'')^2+(y+y'')^2+(z+z'')^2}} \right) \Big|_{x''=-\frac{W_x}{2}}^{\frac{W_x}{2}} \Big|_{y''=-\frac{W_y}{2}}^{\frac{W_y}{2}} \Big|_{z''=-W_z}^0 \quad \#(3.2)$$

$$B_z = -\frac{\delta\Phi_m}{\delta z} = -\frac{M_0}{4\pi} \left(\frac{(y-y'')(x-x'')}{(z-z'')\sqrt{(x+x'')^2+(y+y'')^2+(z+z'')^2}} \right) \Big|_{x''=-\frac{W_x}{2}}^{\frac{W_x}{2}} \Big|_{y''=-\frac{W_y}{2}}^{\frac{W_y}{2}} \Big|_{z''=-W_z}^0 \quad \#(3.3)$$

where B_x, B_y, B_z are the x, y, z components of the magnetic field B respectively, from one cube magnet. The positions of each magnet are then used to translate W_x, W_y, W_z by that amount and the total B field is obtained by adding up the contributions of each component of each magnet respectively.

Appendix A2: Rotation Matrices

$$R_x = [1 \ 0 \ 0 \ 0 \ \cos \cos \theta_x \ \theta_x \ 0 \ \sin \sin \theta_x \ \cos \cos \theta_x \]$$

$$R_y = [\cos \cos \theta_y \ 0 \ \sin \sin \theta_y \ 0 \ 1 \ 0 \ \theta_y \ 0 \ \cos \cos \theta_y \]$$

$$R_z = [\cos \cos \theta_z \ \theta_z \ 0 \ \sin \sin \theta_z \ \cos \cos \theta_z \ 0 \ 0 \ 0 \ 1 \]$$

$$R = [\cos\theta_y\cos\theta_z \ \cos\theta_z\sin\theta_x\sin\theta_y - \cos\theta_x\sin\theta_z \ \cos\theta_x\cos\theta_z\sin\theta_y \\ + \sin\theta_x\sin\theta_z \ \cos\theta_y\sin\theta_z \ \cos\theta_x\cos\theta_z + \sin\theta_x\sin\theta_y\sin\theta_z \ \cos\theta_z\sin\theta_x \\ + \cos\theta_x\sin\theta_y\sin\theta_z - \sin\theta_y \ \cos\theta_y\sin\theta_x \ \cos\theta_x\cos\theta_y \]$$

$$R' = [\cos\theta_y\cos\theta_z \ \cos\theta_y\sin\theta_z - \sin\theta_y \ \cos\theta_z\sin\theta_x\sin\theta_y - \cos\theta_x\sin\theta_z \ \cos\theta_x\cos\theta_z \\ + \sin\theta_x\sin\theta_y\sin\theta_z \ \cos\theta_y\sin\theta_x \ \cos\theta_x\cos\theta_z\sin\theta_y + \sin\theta_x\sin\theta_z \ \cos\theta_z\sin\theta_x \\ + \cos\theta_x\sin\theta_y\sin\theta_z \ \cos\theta_x\cos\theta_y \]$$

Appendix B: Mathematical Derivations

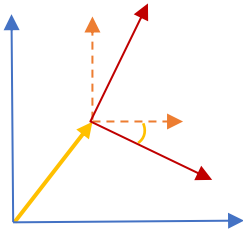


Figure 9. Coordinate system

We first define the coordinate systems as in Fig 9.

The magnetic field generated by the neodymium magnets is described by Gauss's law for magnetism, respectively:

$$\nabla \cdot B = \nabla \cdot \mu_0 H = 0 \quad (9)$$

where H is the magnetic field intensity, μ_0 is the permeability of free space and B is the magnetic field vector.

The general solution to this for magnetostatics is well known:

$$B = \mu_0 H = -\mu_0 \nabla \Phi_m \quad (10)$$

We can then solve it numerically within our boundary conditions as laid out in our experimental setup. However, due to the computational power required to solve such complex equations, this would be extremely and unnecessarily time consuming.

We hence utilise the magnetic equivalent of Poisson's equation:

$$\Phi_m = \frac{\nabla \cdot \iiint \frac{M(r'')}{|r - r''|} dr'' \quad (11)$$

where Φ_m is the magnetic scalar potential, M is the magnetisation vector of the magnet, r is the observation point in Cartesian coordinates of the lab frame and r'' is a point on the magnet. Substituting the dimensions and position of the magnet, as well as the vertical direction of the poles, equation (1) simplifies to

$$\Phi_m(x, y, z) = \frac{M_0}{\pi} \int_{-\frac{W_x}{2}}^{\frac{W_x}{2}} \int_{-\frac{W_y}{2}}^{\frac{W_y}{2}} \frac{1}{|r - r''|} dy'' dx'' \Big|_{z''=-W_z} \quad (2)$$

where W_x , W_y and W_z are the respective lengths of the magnet in x , y , z coordinates. By taking the negative gradient of Φ_m as laid out in (10), we can cancel out the respective integrals and the equation for magnetic field simplifies to:

To characterise the magnetisation M of the magnet, the magnetic field strength at different distances from the magnet were determined experimentally.

Using the definition of the magnetic potential energy density, we get:

$$u_m(x, y, z) = -\frac{\chi v}{2\mu_0} (B_x^2 + B_y^2 + B_z^2) \quad (12)$$

To obtain total magnetic potential energy, this is integrated over the volume of the graphite sheet, and to define the Euler angles in the three dimensions, intrinsic rotations were done using the Davenport Rotation Matrix (Refer to Appendix B), obtaining:

$$\begin{aligned} U_m(s_x, s_y, s_z, \theta_x, \theta_y, \theta_z) &= \int_{-\frac{L_x}{2}}^{\frac{L_x}{2}} \int_{-\frac{L_y}{2}}^{\frac{L_y}{2}} \int_0^{L_z} u_m(x, y, z) dz' dy' dx' \quad (13) \\ &= (z' \sin \sin \theta_x - y' \cos \cos \theta_x) \sin \sin \theta_z \\ &+ (x' \cos \cos \theta_y + (z' \cos \cos \theta_x + y' \sin \sin \theta_x) \sin \sin \theta_y) \cos \cos \theta_z \\ &+ s_x y \\ &= \cos \cos \theta_z (y' \cos \cos \theta_x - z' \sin \sin \theta_x) + x' \cos \cos \theta_y \sin \sin \theta_z \\ &+ (z' \cos \cos \theta_x + y' \sin \sin \theta_x) \sin \sin \theta_y \sin \sin \theta_z z \\ &= (z' \cos \cos \theta_x + y' \sin \sin \theta_x) \cos \cos \theta_y - x' \sin \sin \theta_y + s_z \end{aligned}$$

where L_x , L_y and L_z are the respective lengths of the graphite plate, s_x , s_y and s_z are the respective lateral displacements of the centre of the graphite plate and θ_x , θ_y and θ_z are the rotations in the respective axes.

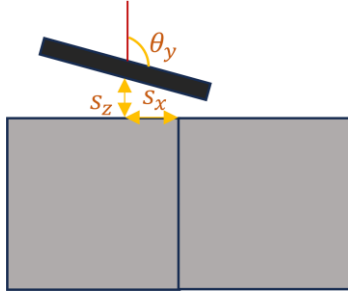


Figure 10.1 Side view displacement

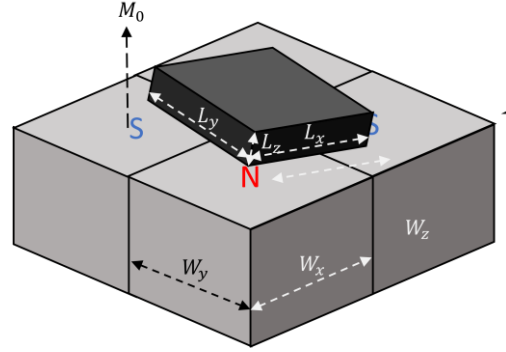


Figure 10.2 Definitions of dimensions

However, to account for anisotropy, the x, y, z component of susceptibility χ_v is multiplied by the respective B field component. The components of the B field would also have to be reverse rotated back into the lab frame using the transposed rotation matrix, obtaining:

$$\begin{aligned}
 u_m(x, y, z, \theta_x, \theta_y, \theta_z) &= -\frac{1}{2\mu_0} (\chi_x B_x'^2 + \chi_y B_y'^2 + \chi_z B_z'^2) \#(5) B_x' \\
 &= B_x \cos \cos \theta_y \cos \cos \theta_z - B_z \sin \sin \theta_y + B_y \cos \cos \theta_y \sin \sin \theta_z B_y' \\
 &= B_z \cos \theta_y \sin \sin \theta_x \\
 &+ B_x (\cos \cos \theta_z \sin \sin \theta_x \sin \sin \theta_y - \cos \cos \theta_x \sin \sin \theta_z) \\
 &+ B_y (\cos \cos \theta_x \cos \cos \theta_z + \sin \sin \theta_x \sin \sin \theta_y \sin \sin \theta_z) B_z' \\
 &= B_z \cos \cos \theta_x \cos \cos \theta_y \\
 &+ B_x (\cos \cos \theta_x \cos \cos \theta_z \sin \sin \theta_y + \sin \sin \theta_x \sin \sin \theta_z) + B_y (- \\
 &\cos \cos \theta_z \sin \sin \theta_x + \cos \cos \theta_x \sin \sin \theta_y \sin \sin \theta_z)
 \end{aligned}$$

Appendix C: Magnetic field fit

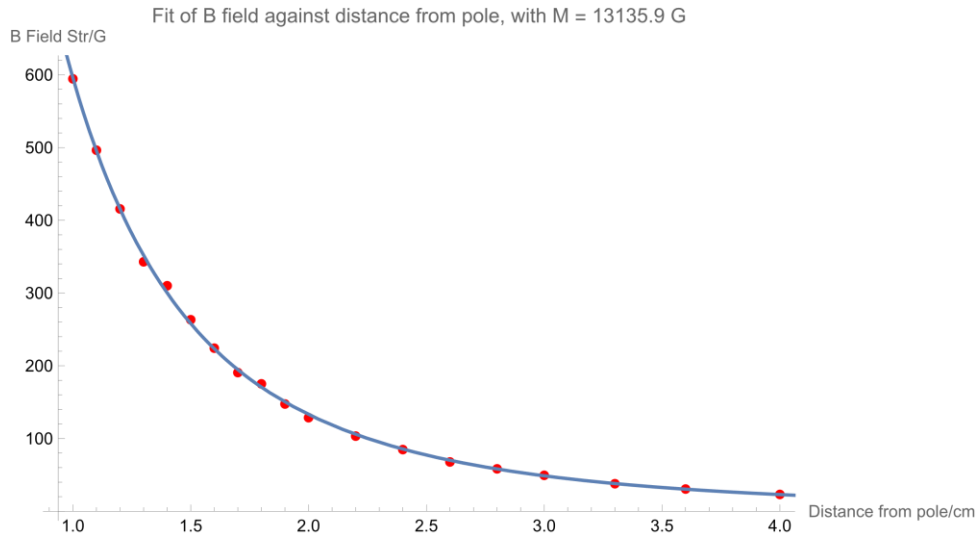


Figure 11. Magnetic field fit to experimentally derived field magnitude measurements at certain distance intervals from magnets

Appendix D: Mathematical Proof for harmonic motion

We first determining of magnitudes of the first 5 terms of the Taylor series around the various degrees of freedom at the equilibrium point:

$$f(a) = f(a) + \frac{f'(a)}{1!}(x - a) + \frac{f''(a)}{2!}(x - a)^2 + \frac{f'''(a)}{3!}(x - a)^3 + \frac{f''''(a)}{4!}(x - a)^4 \#(9)$$

where a is equilibrium position of the respective degree of freedom and x is the amplitude of oscillation. Since the 3rd and 4th order terms are significantly lower than the 2nd order term for all modes of oscillation, we conclude that it is indeed simple harmonic.

Appendix E Characteristics of graphite sheet

Table 1. Graphite characteristics

Index	L_x/mm	L_y/mm	L_z/mm	m/mg	s_z/mm	$\chi_{x,y}(SI)$	$\chi_z(SI)$
Isostatic							
1	3.8	3.8	0.272	6.6	0.432	-1.379×10^{-4}	
2	5.3	5.3	0.361	17.3	0.482		
3	5.8	5.8	0.242	13.6	0.586		
4	7.5	7.5	0.395	37.8	0.598		
5	10.0	10.0	0.312	52.3	Unstable		
Pyrolytic							
6	5.3	5.3	0.351	19.7	0.684	-6.92×10^{-5}	-41.1×10^{-5}
7	7.5	7.5	0.458	39.2	0.875		
8	10.0	10.0	0.458	71.5	0.925		

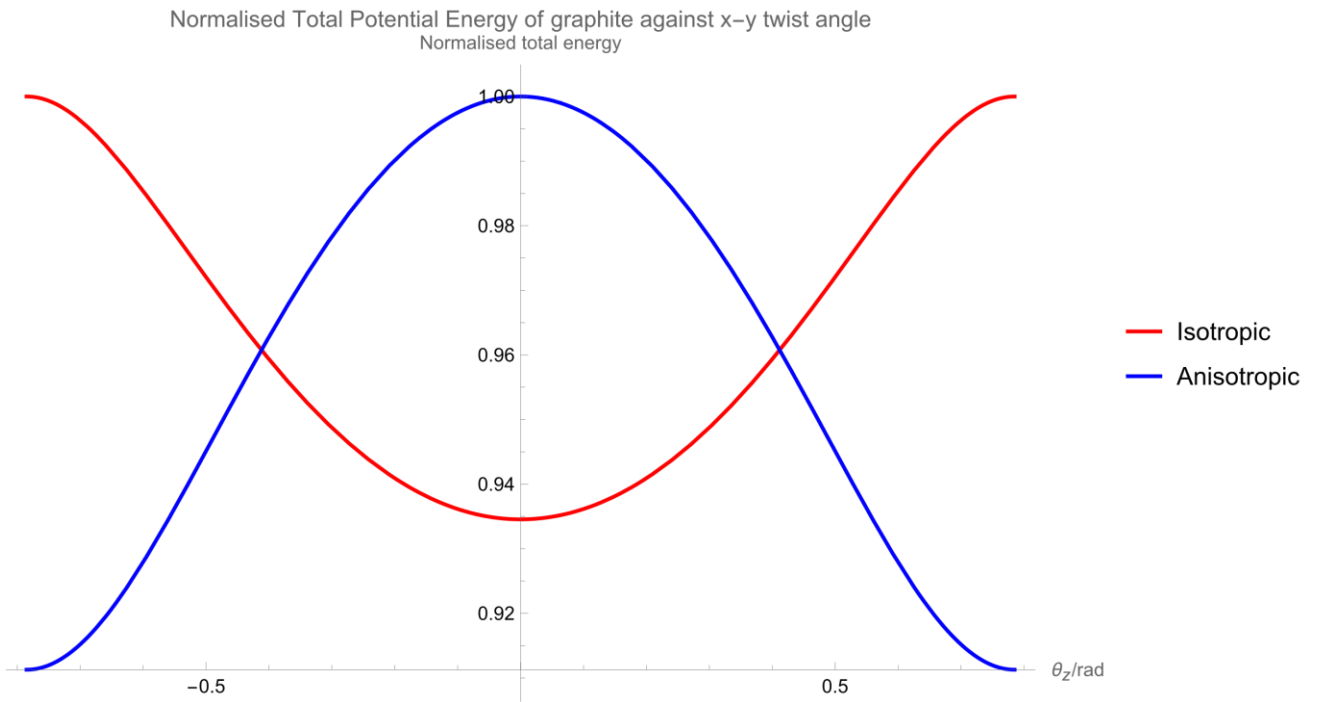


Figure 12. Normalised graph of the theoretical total potential energy of graphite against the x-y twist angle ϑ_x in radians of the graphite sheet for isotropic and anisotropic graphite. The graph was normalised by dividing each graph by its max value

Appendix F Levitation force to levitation height fit

Levitation force against levitation height for pyrolytic graphite

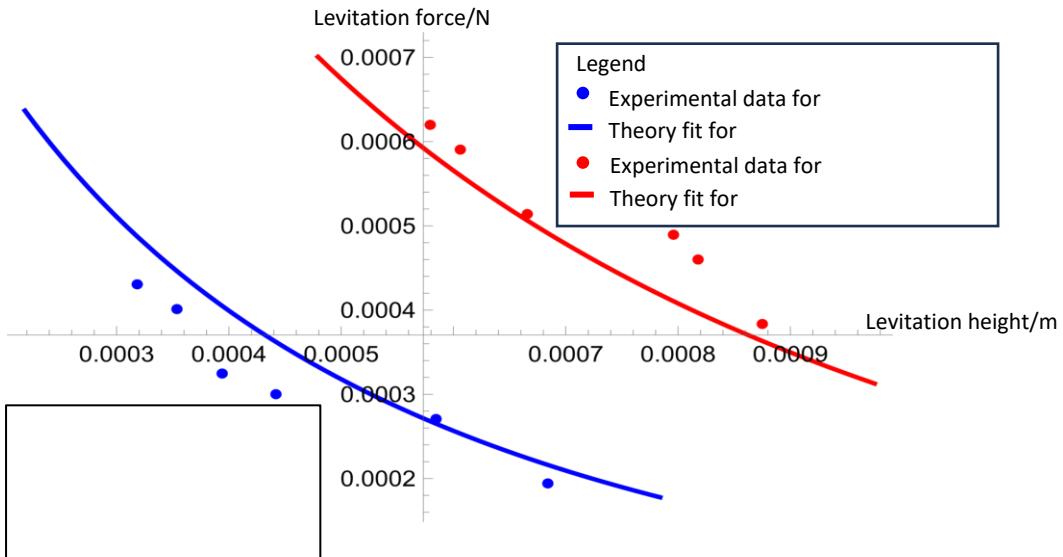


Figure 13 Fit of levitation force against levitation height for susceptibility for anisotropic graphite

Appendix F Eigenvectors and Frequencies of different modes of oscillation of graphite sheets

Table 2. Theoretical frequencies and their corresponding eigenvectors of anisotropic graphite, $L_{x,y} = 7.5$ mm

Frequencies	x	y	z	θ_x	θ_y	θ_z	Mode
19.583	0	0	-1	0	0	0	Vertical
17.262	0.054	0.012	0	-0.532	-0.845	0	Tip/tilt
17.262	-0.012	0.054	0	0.845	-0.532	0	Tip/tilt
7.402	0	0	0	0	0	1	Twist
4.797	0.783	-0.62	0	0.055	0.006	0	Lateral x-y
4.797	-0.62	-0.783	0	0.006	-0.055	0	Lateral x-y

Table 3. Theoretical frequencies and their corresponding eigenvectors of isotropic graphite, $L_{x,y} = 7.5$ mm

	x	y	z	θ_x	θ_y	θ_z	Mode
18.28	0	0	1	0	0	0	Vertical
15.817	-0.015	-0.014	0	-0.695	0.719	0	Tip/tilt
15.817	0.014	-0.015	0	-0.719	-0.695	0	Tip/tilt
3.462	0	0	0	0	0	1	Twist
2.307	-0.66	-0.751	0	0.015	-0.013	0	Lateral x-y
2.306	0.751	-0.66	0	0.013	0.015	0	Lateral x-y

Table 4. Theoretical frequencies and their corresponding eigenvectors of anisotropic graphite, $L_{x,y} = 5.3$ mm

Frequencies	x	y	z	θ_x	θ_y	θ_z	Mode
22.016	0	0	-1	0	0	0	Vertical
19.343	-0.014	-0.066	0	-0.538	0.84	0	Tip/tilt
19.343	0.066	-0.014	0	-0.84	-0.538	0	Tip/tilt
9.28	0	0	0	0	0	1	Twist
6.715	0.694	-0.717	0	0.067	-0.001	0	Lateral x-y
6.715	0.717	0.694	0	0.001	0.067	0	Lateral x-y

Table 5. Theoretical frequencies and their corresponding eigenvectors of isotropic graphite, $L_{x,y} 5.3$ mm

	x	y	z	θ_x	θ_y	θ_z	Mode
20.162	0	0	-1	0	0	0	Vertical
18.242	0.018	0.035	0	-0.886	0.461	0	Tip/tilt
18.242	-0.035	0.018	0	-0.461	-0.886	0	Tip/tilt
4.45	0	0	0	0	0	1	Twist
4.119	-0.642	-0.766	0	-0.03	0.025	0	Lateral x-y
4.119	0.766	-0.642	0	-0.025	-0.03	0	Lateral x-y

Table 6. Theoretical frequencies and their corresponding eigenvectors of anisotropic graphite, $L_{x,y} = 10$ mm

Frequencies	x	y	z	θ_x	θ_y	θ_z	Mode
17.89	0	0	1	0	0	0	Vertical
15.978	-0.004	0.044	0	0.774	-0.631	0	Tip/tilt
15.978	0.044	0.004	0	-0.631	-0.774	0	Tip/tilt
6.103	0	0	0	0	0	1	Twist
3.484	0.942	-0.334	0	0.04	0.019	0	Lateral x-y
3.483	0.334	0.942	0	-0.019	0.04	0	Lateral x-y

Table 7. Theoretical frequencies and their corresponding eigenvectors of isotropic graphite, $L_{x,y} 5.8$ mm

	x	y	z	θ_x	θ_y	θ_z	Mode
19.397	0	0	-1	0	0	19.397	Vertical
17.203	-0.01	-0.016	0	0.85	-0.526	17.203	Tip/tilt

17.203	-0.016	0.01	0	-0.526	-0.85	17.203	Tip/tilt
4.127	0	0	0	0	0	4.127	Twist
3.603	-0.711	-0.703	0	-0.013	0.013	3.603	Lateral x-y
3.603	0.703	-0.711	0	-0.013	-0.013	3.603	Lateral x-y

Table 8. Theoretical frequencies and their corresponding eigenvectors of isotropic graphite, $L_{x,y} = 3.8 \text{ mm}$

	x	y	z	θ_x	θ_y	θ_z	Mode
22.158	0	0	1	0	0	22.158	Vertical
20.845	-0.076	0.085	0	-0.74	-0.663	20.845	Tip/tilt
20.845	0.085	0.076	0	-0.663	0.74	20.845	Tip/tilt
5.915	-0.367	-0.923	0	-0.106	0.042	5.915	Lateral x-y
5.915	0.923	-0.367	0	-0.042	-0.106	5.915	Lateral x-y
5.331	0	0	0	0	0	5.331	Twist

Appendix G FFT Graphs with theory fits

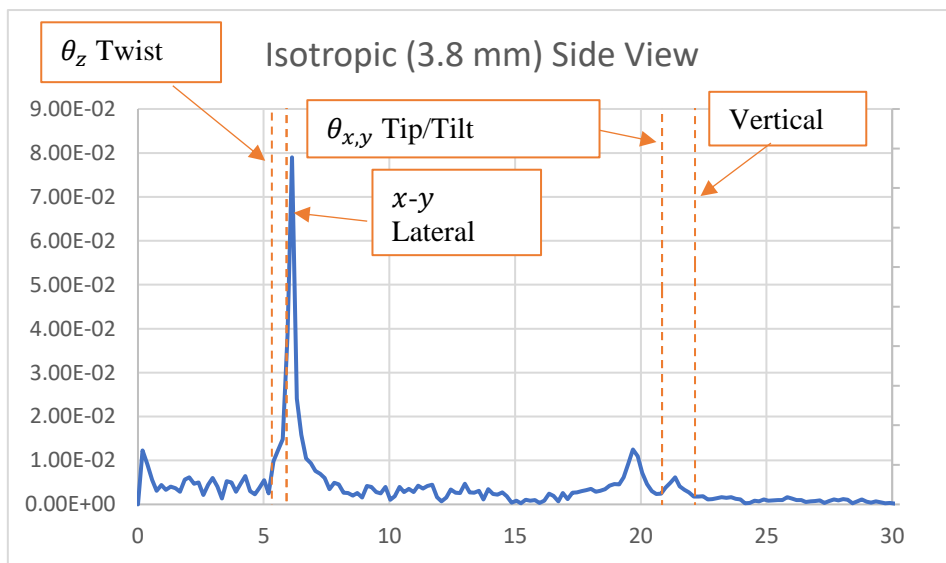


Figure 14.1. FFT of side view tracked motion of Isotropic graphite of $L_{x,y} = 3.8 \text{ mm}$

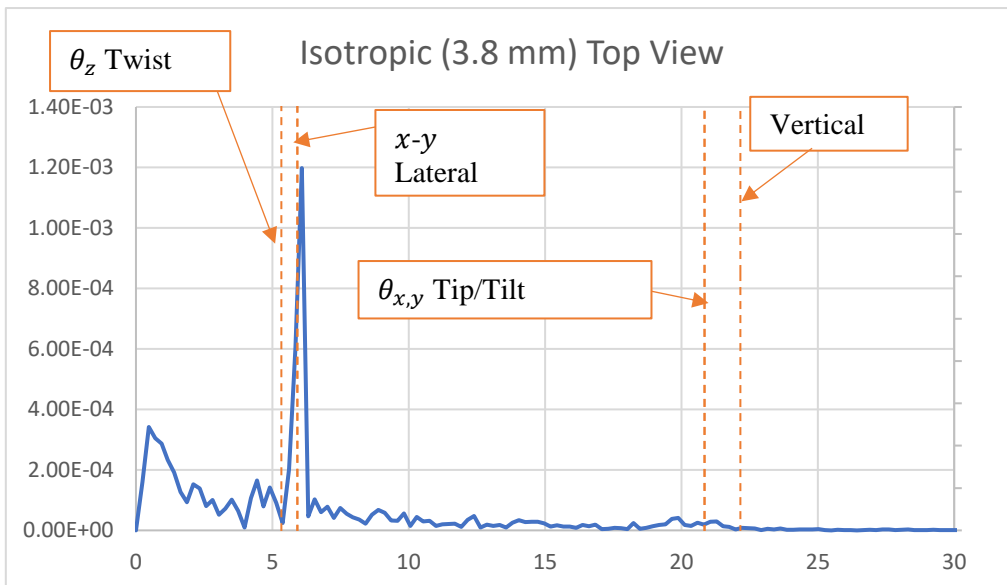


Figure 14.2. FFT of top view tracked motion of Isotropic graphite of $L_{x,y} = 3.8 \text{ mm}$

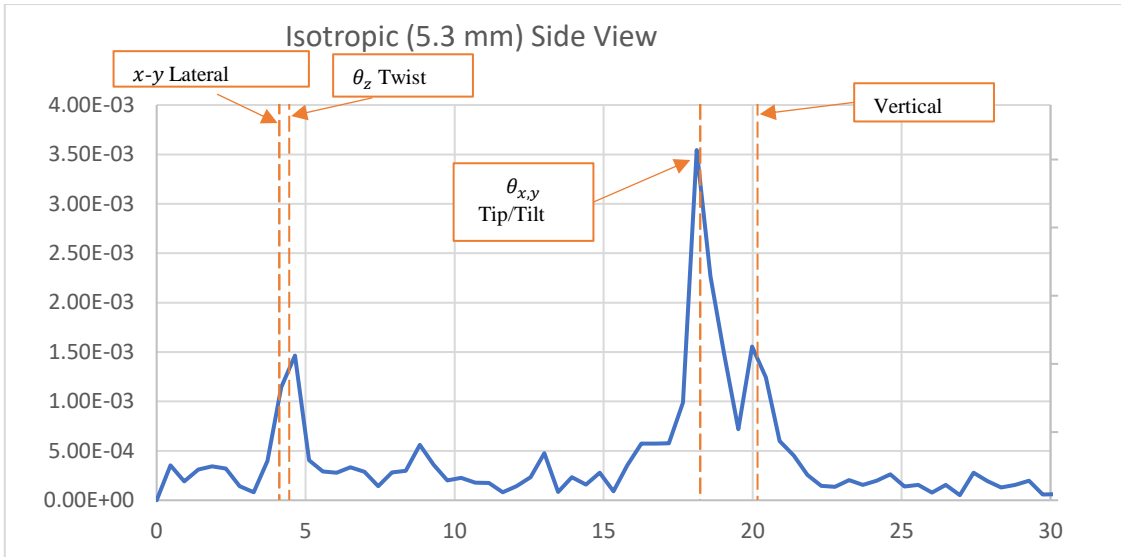


Figure 15.1 FFT of side view tracked motion of Isotropic graphite of $L_{x,y} = 5.3$ mm

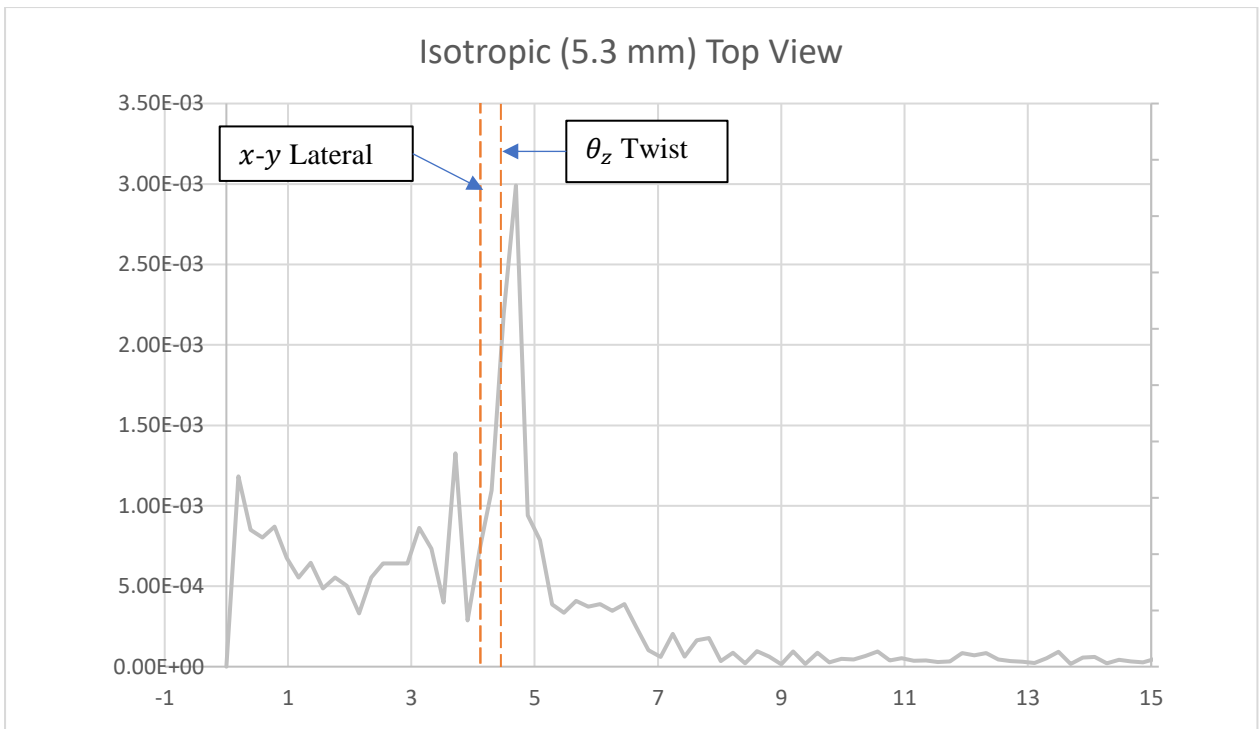


Figure 15.2. FFT of top view tracked motion of Isotropic graphite of $L_{x,y} = 5.3$ mm

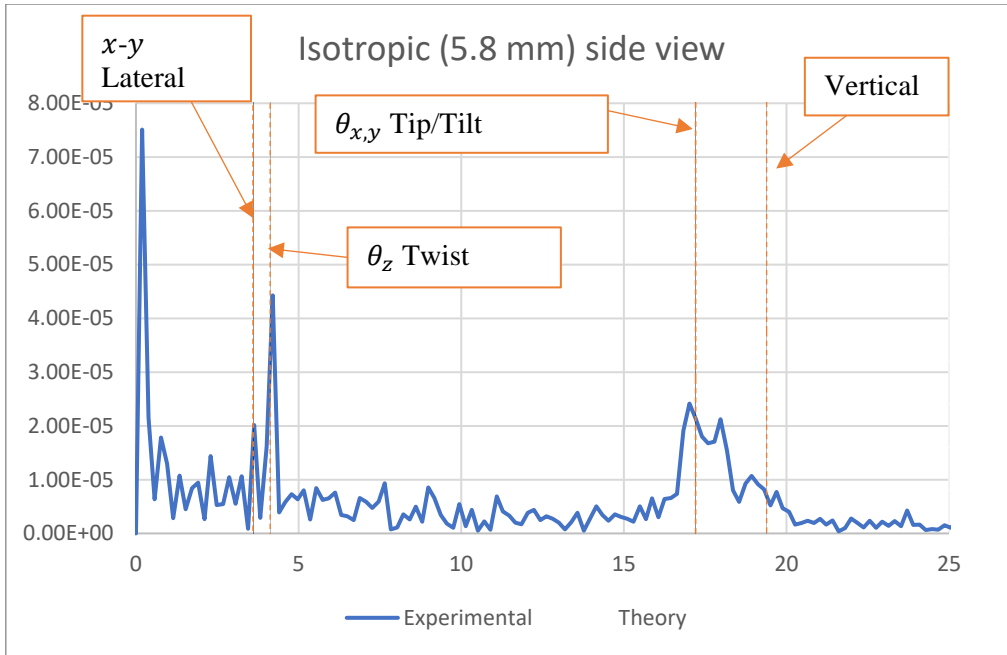


Figure 16.1 FFT of side view tracked motion of Isotropic graphite of $L_{x,y} = 5.8$ mm

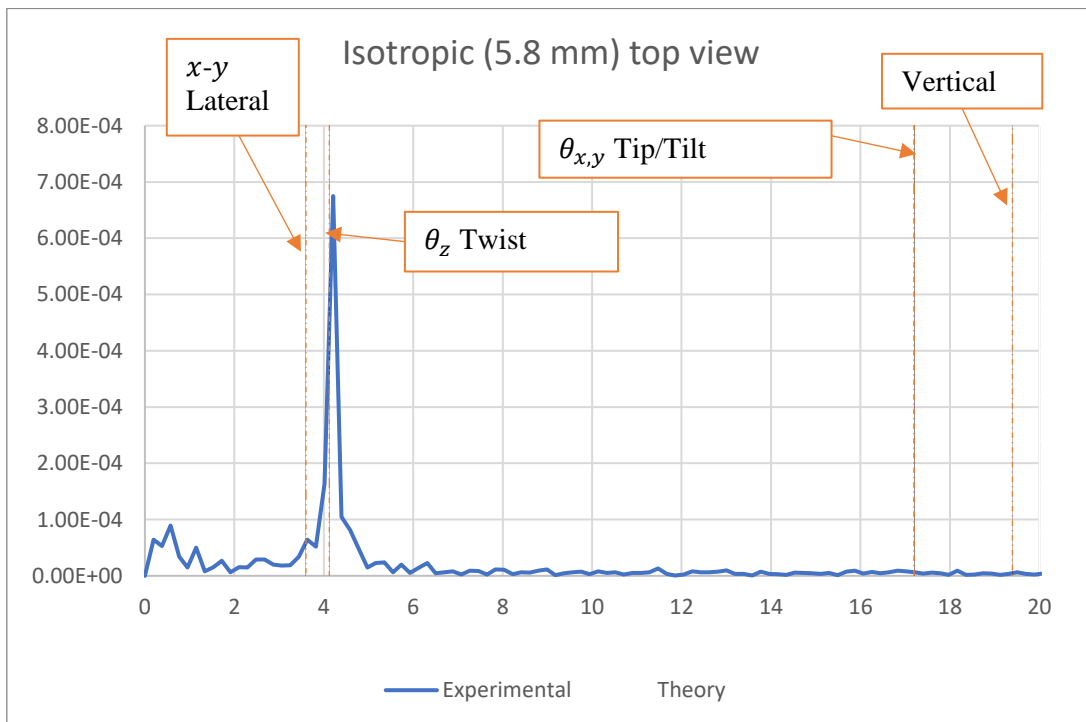


Figure 16.2 FFT of top view tracked motion of Isotropic graphite of $L_{x,y} = 5.8$ mm

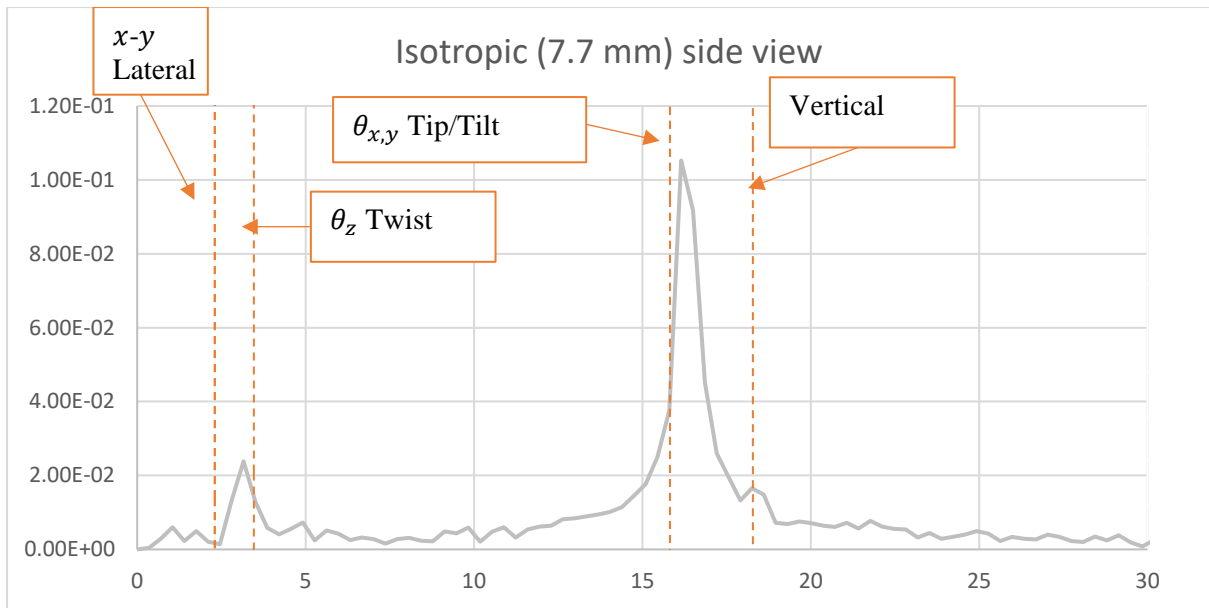


Figure 17.1. FFT of side view tracked motion of Isotropic graphite of $L_{x,y} = 7.7$ mm

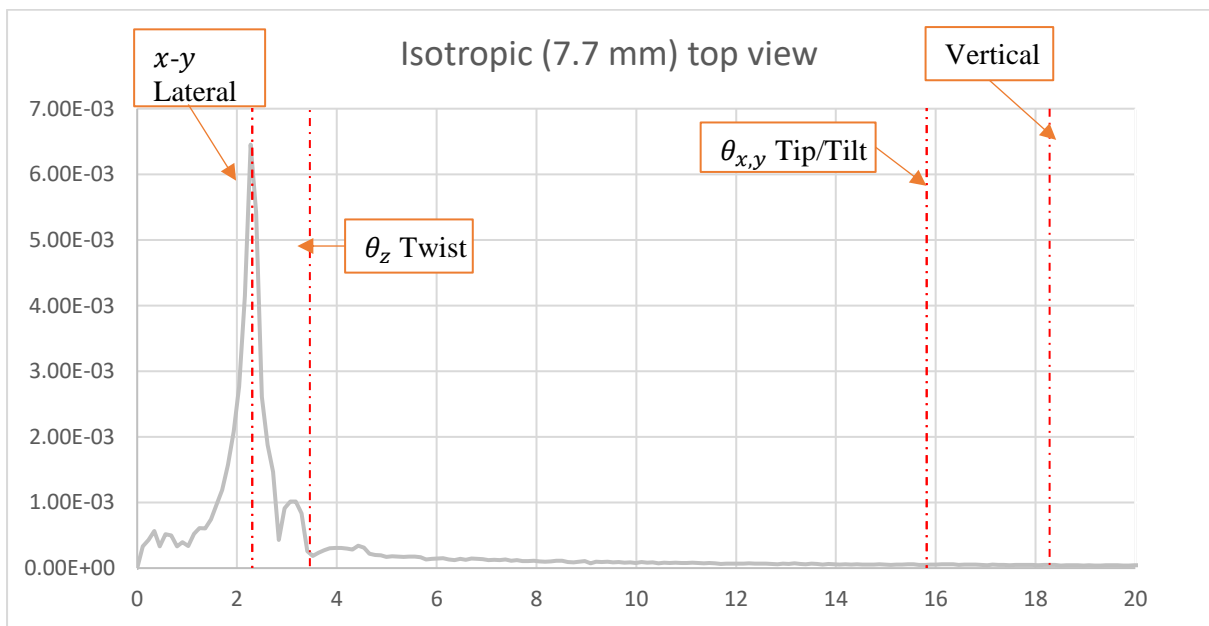


Figure 17.2. FFT of top view tracked motion of Isotropic graphite of $L_{x,y} = 7.7$ mm

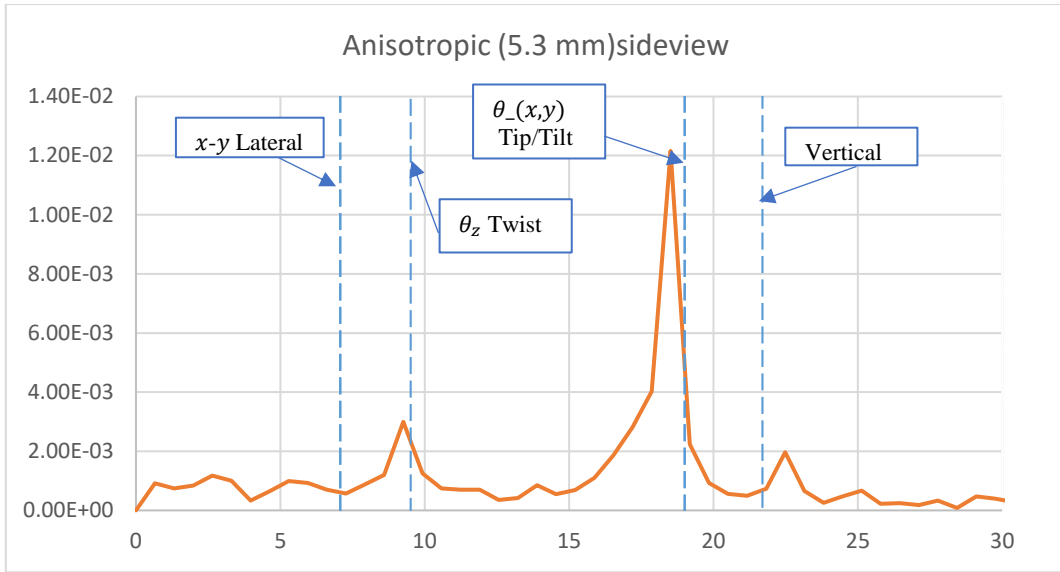


Figure 18.1. FFT of side view tracked motion of anisotropic graphite of $L_{x,y}=5.3$ mm

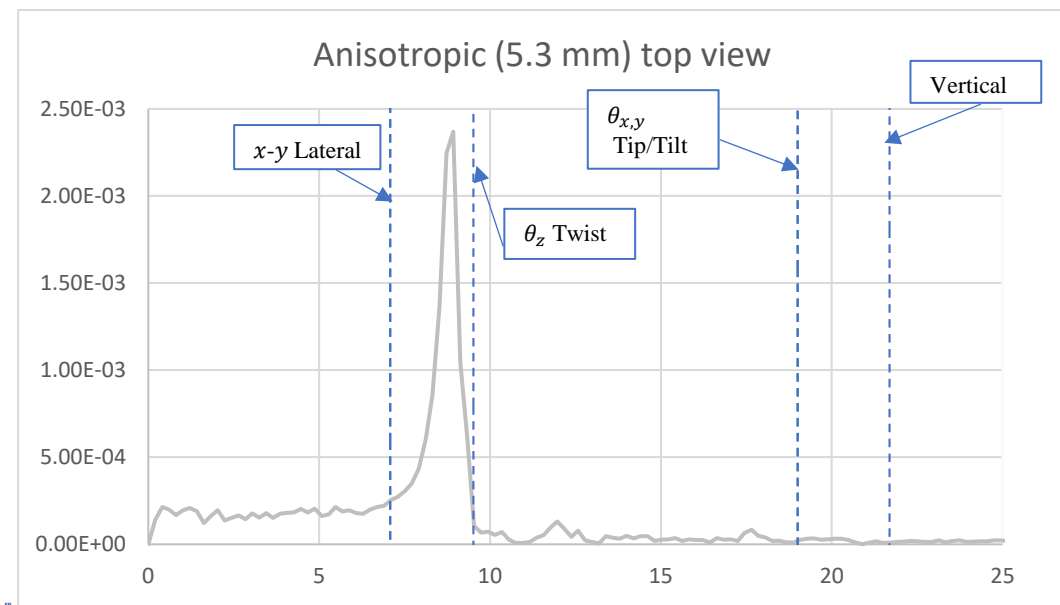


Figure 18.2. FFT of top view tracked motion of anisotropic graphite of $L_{x,y}=5.3$ mm

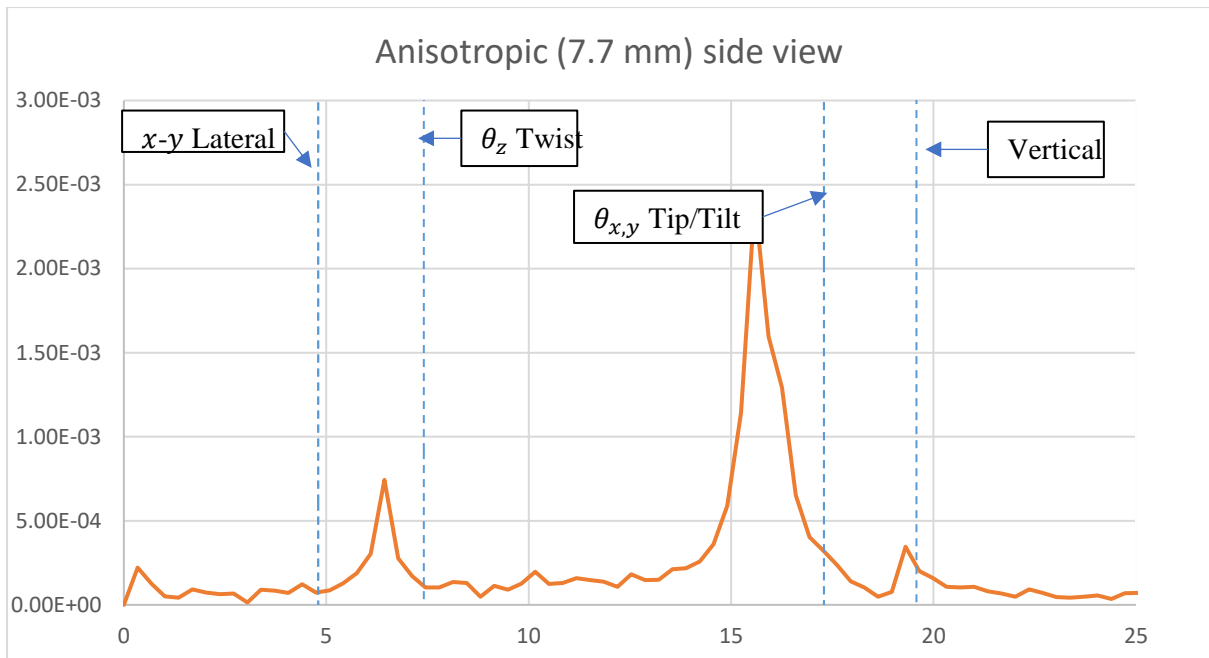


Figure 19.1. FFT of side view tracked motion of anisotropic graphite of $L_{x,y}=7.7$ mm

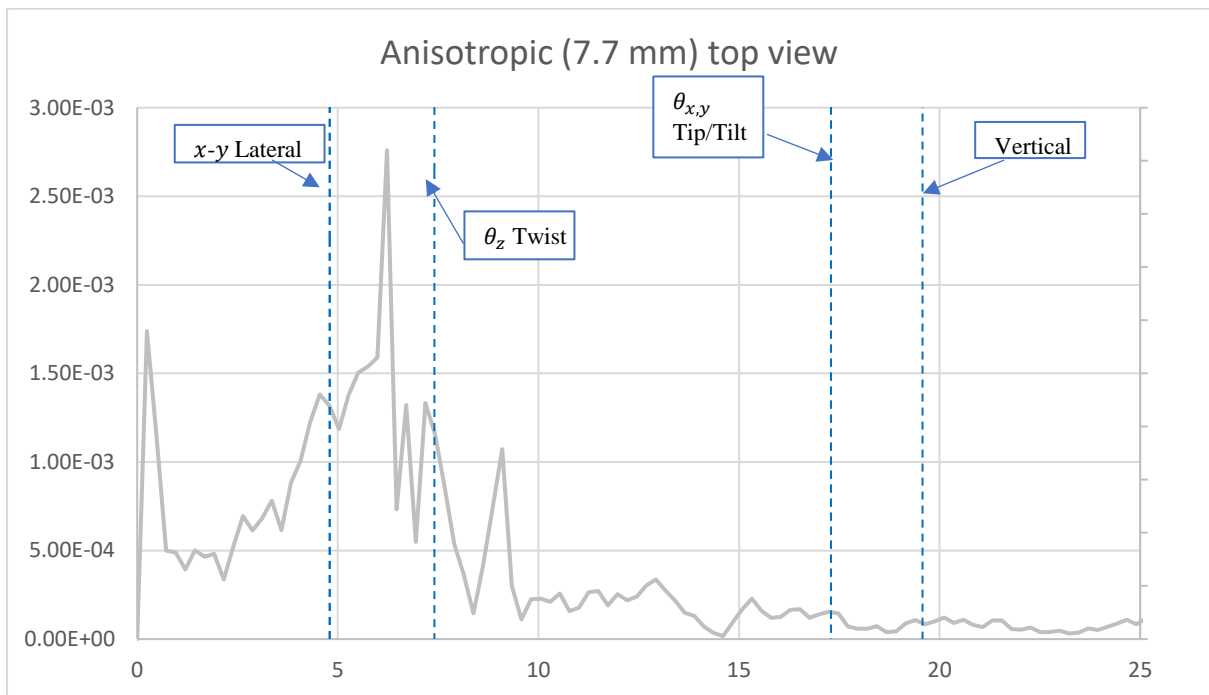


Figure 19.2. FFT of top view tracked motion of anisotropic graphite of $L_{x,y}=7.7$ mm

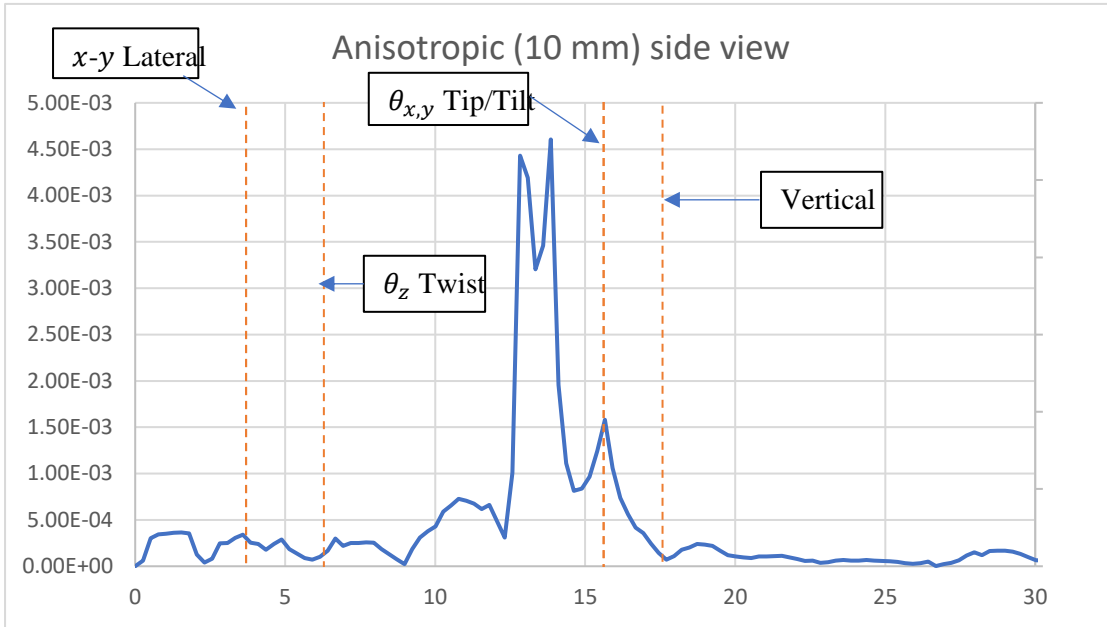


Figure 20.1. FFT of side view tracked motion of anisotropic graphite of $L_{x,y}=10$ mm

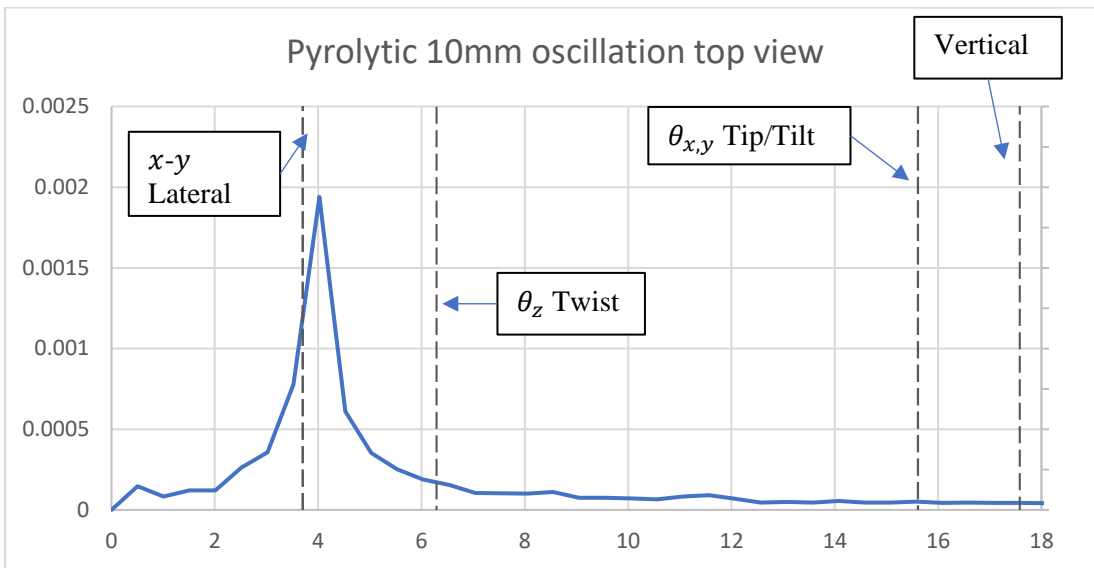


Figure 20.2. FFT of top view tracked motion of anisotropic graphite of $L_{x,y}=10$ mm

Appendix H

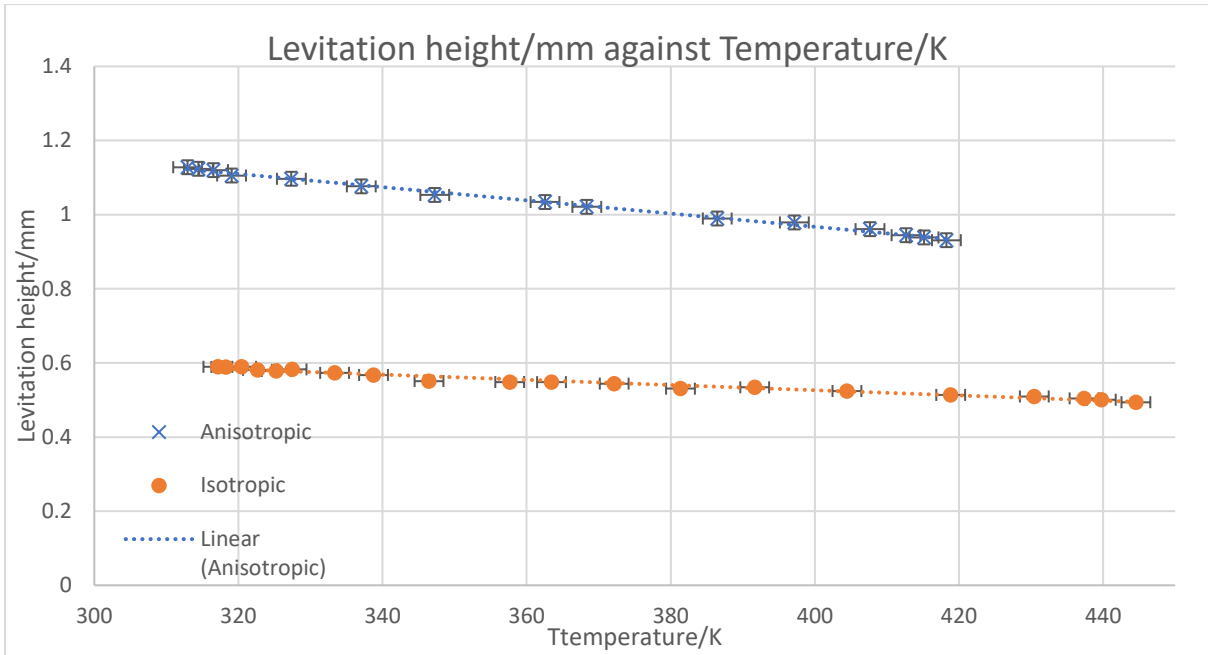


Figure 21. Levitation height against temperature

Appendix I: relation between sheet size and resonant frequencies

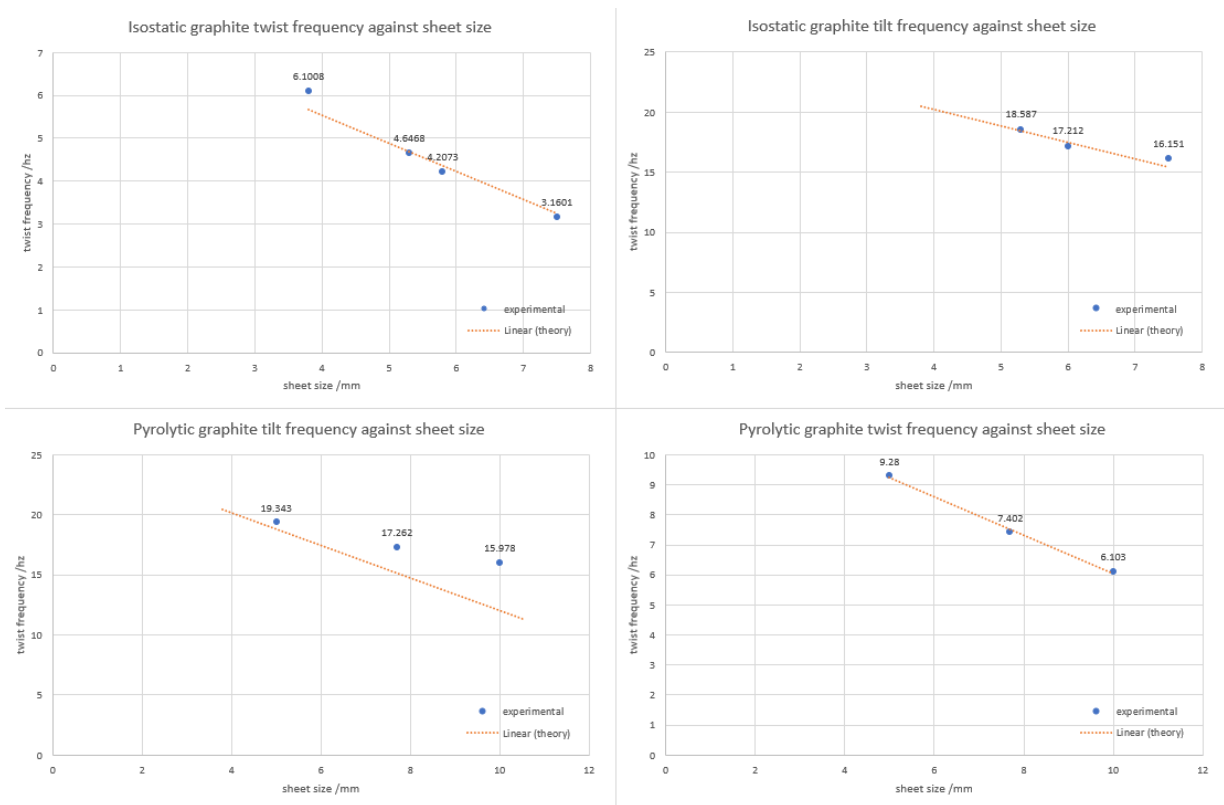
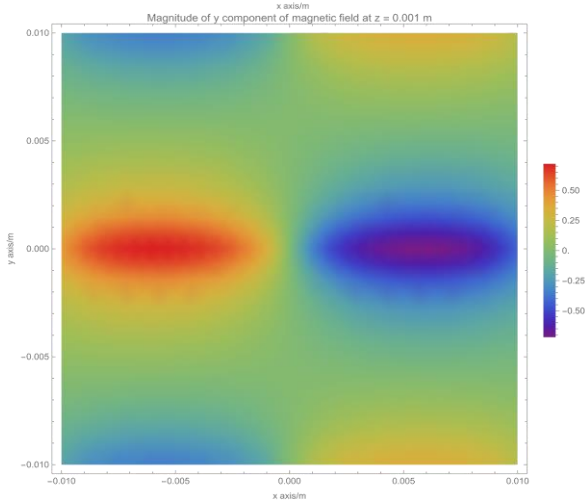
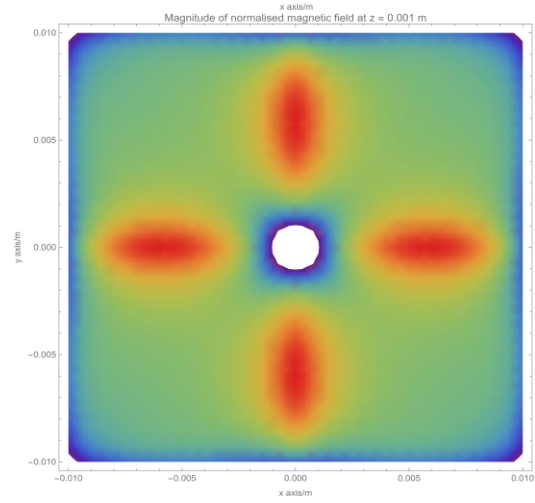
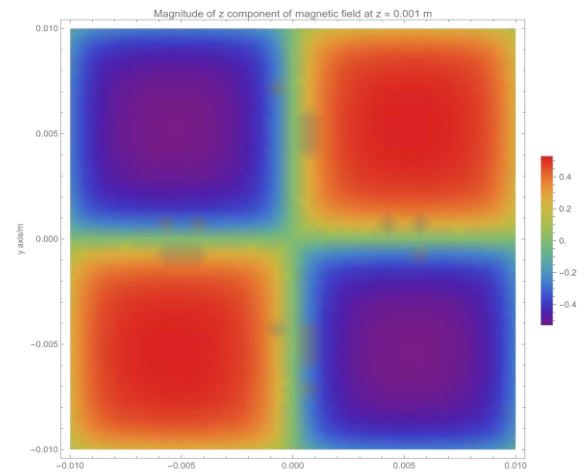
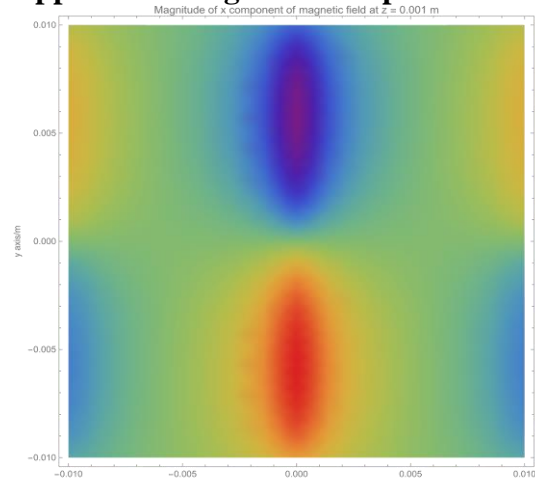


Figure 22. Tilt and twist frequencies against sheet size for pyrolytic and isostatic graphite.

Appendix J Magnetic field plots



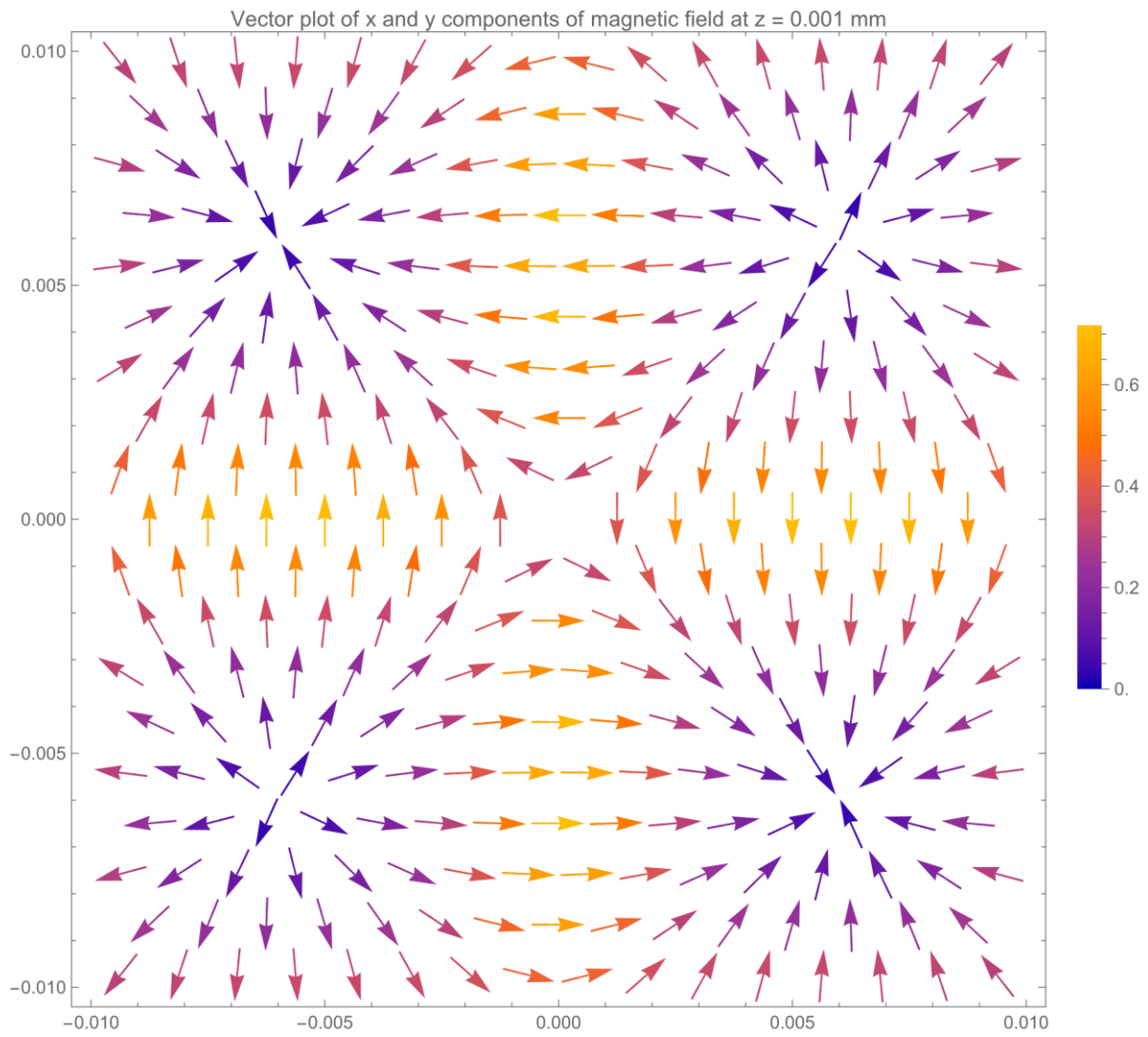


Figure 24. Magnetic field X and Y component vector plot

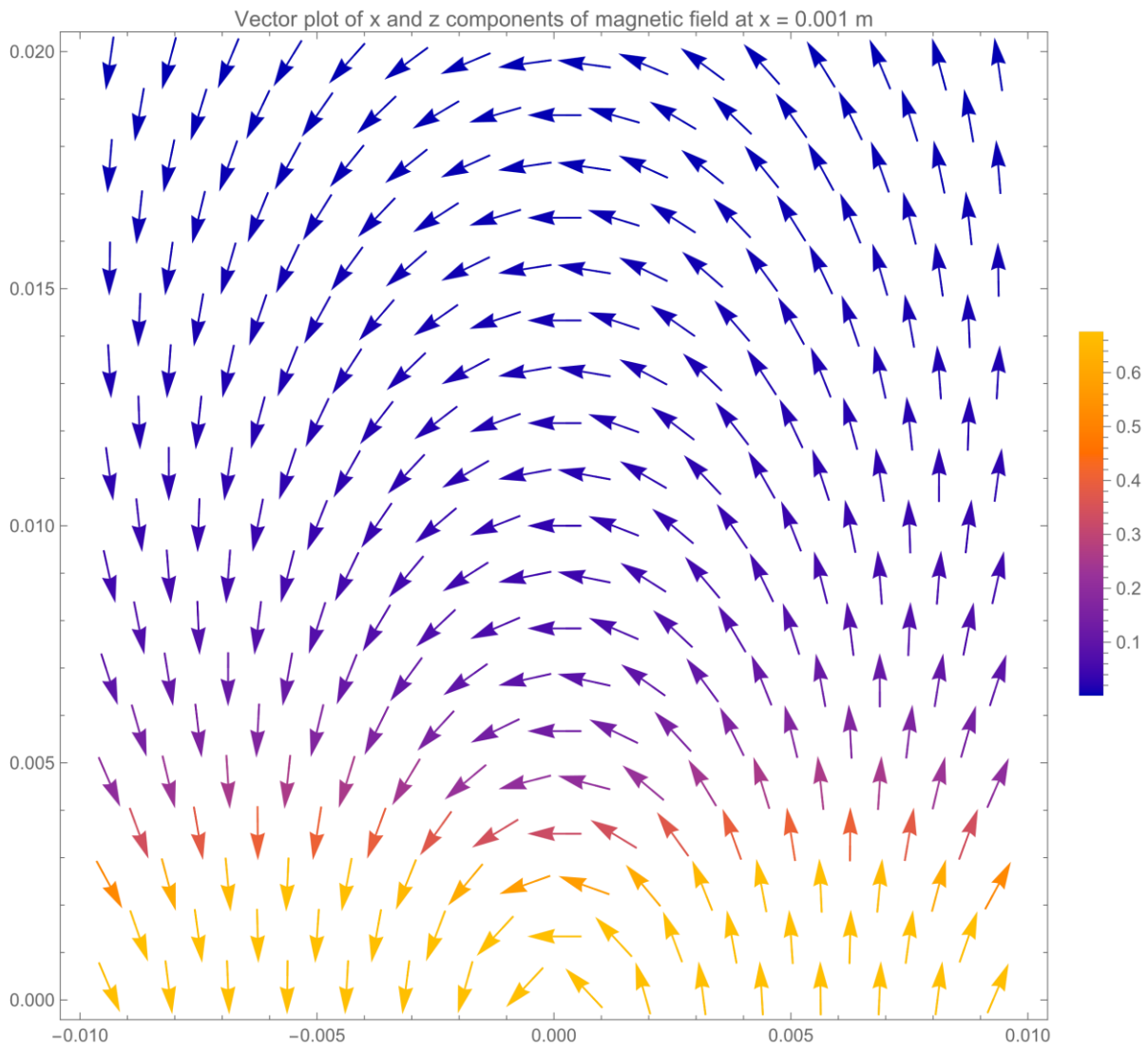


Figure 25. Magnetic field X and Z component vector plot

Appendix I Theoretical relationships with length of sheet

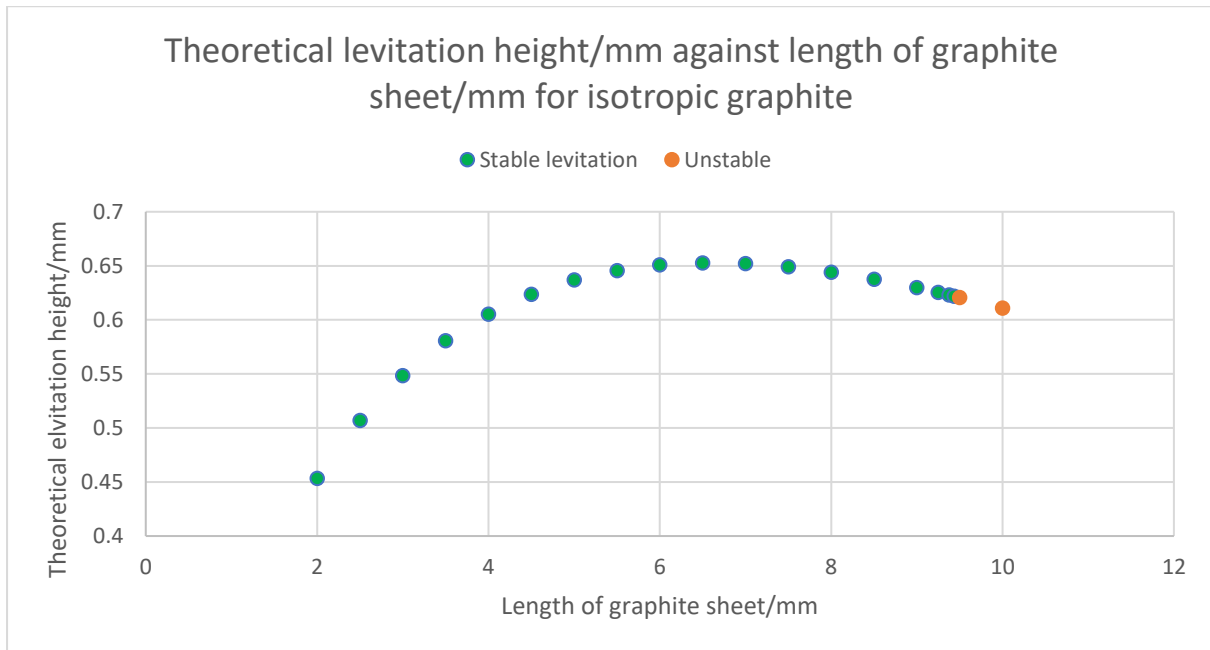


Figure 26. Theoretical levitation height/mm against length of graphite sheet/mm for isotropic graphite using susceptibility values laid out Table 1. For the isotropic graphite. b

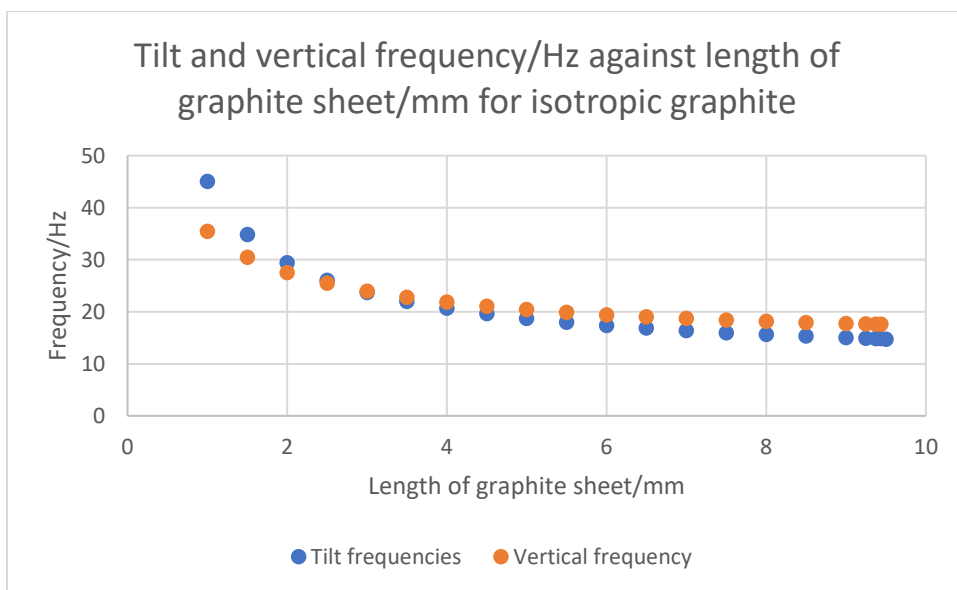


Figure 27. Theoretical tilt and vertical frequencies against length of graphite sheet using susceptibility values laid out in Table 1. For isotropic graphite.

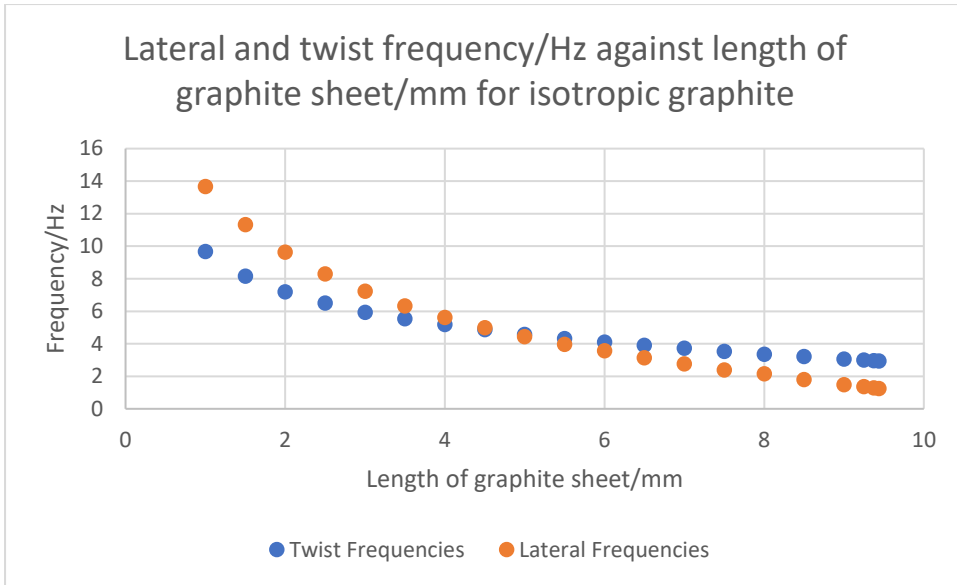


Figure 28. Theoretical tilt and vertical frequencies against length of graphite sheet using susceptibility values laid out in Table 1. For isotropic graphite.

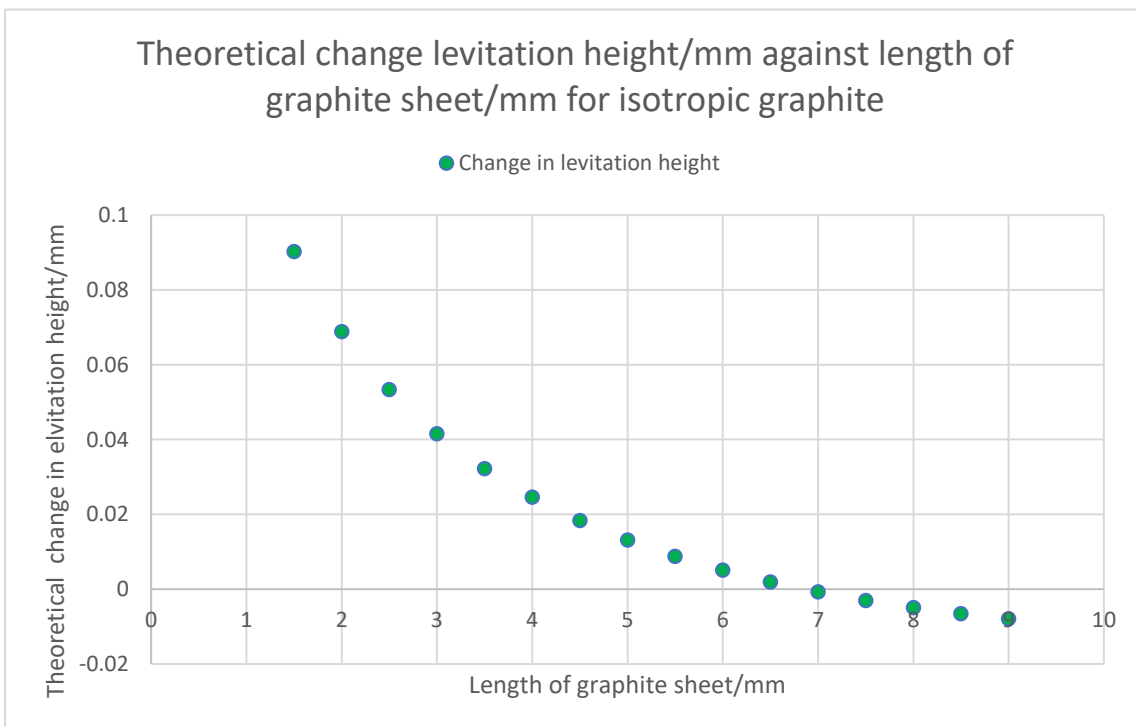


Figure 29. Theoretical tilt and vertical frequencies against length of graphite sheet using susceptibility values laid out in Table 1. For isotropic graphite.

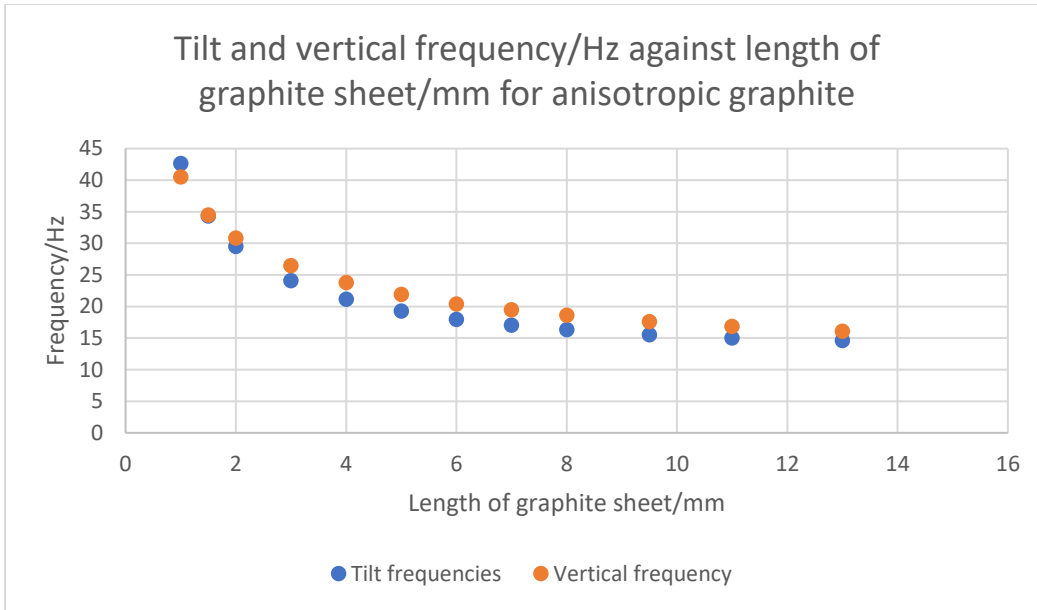


Figure 30 Tilt and vertical frequency against length of graphite sheet for anisotropic graphite (theory)

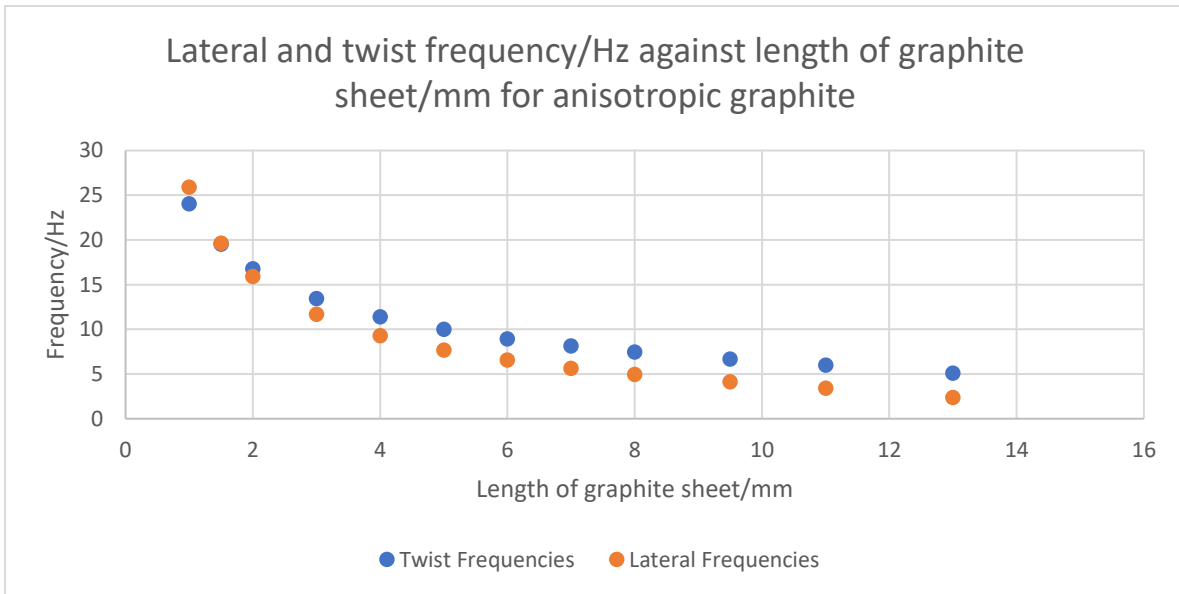


Figure 31. Lateral and twist frequency against length of sheet for anisotropic graphite (theory)

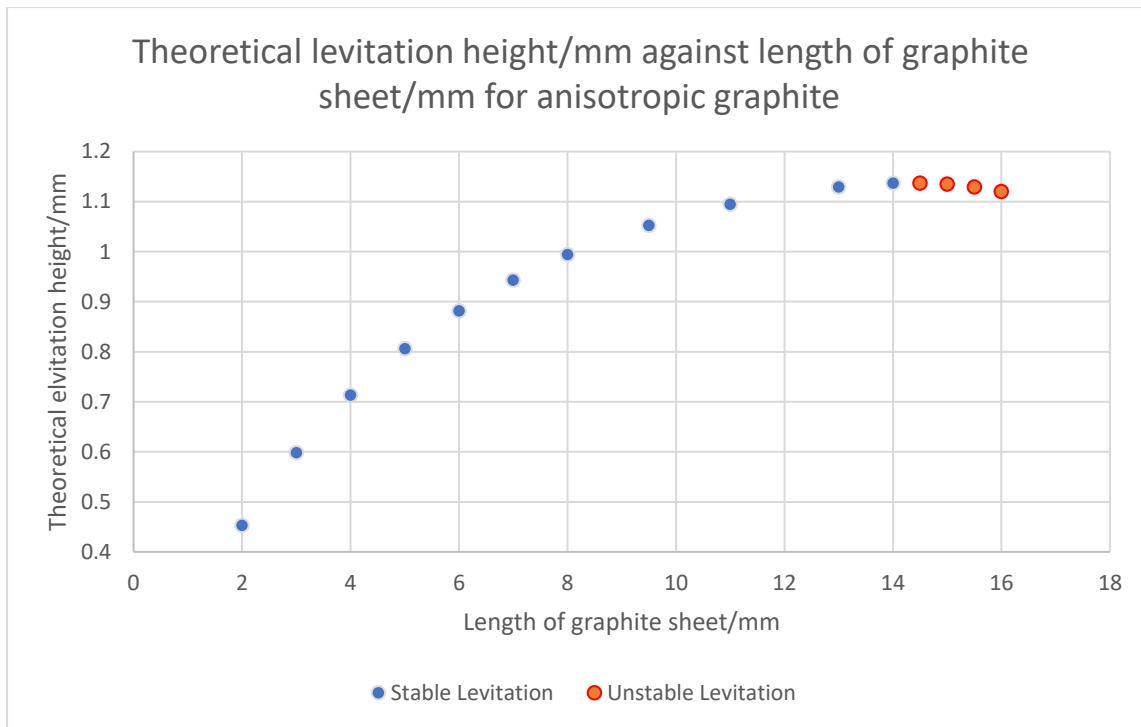


Figure 32. Theoretical levitation height/mm against length of graphite sheet/mm for isotropic graphite using susceptibility values laid out Table 1. For the anisotropic graphite.

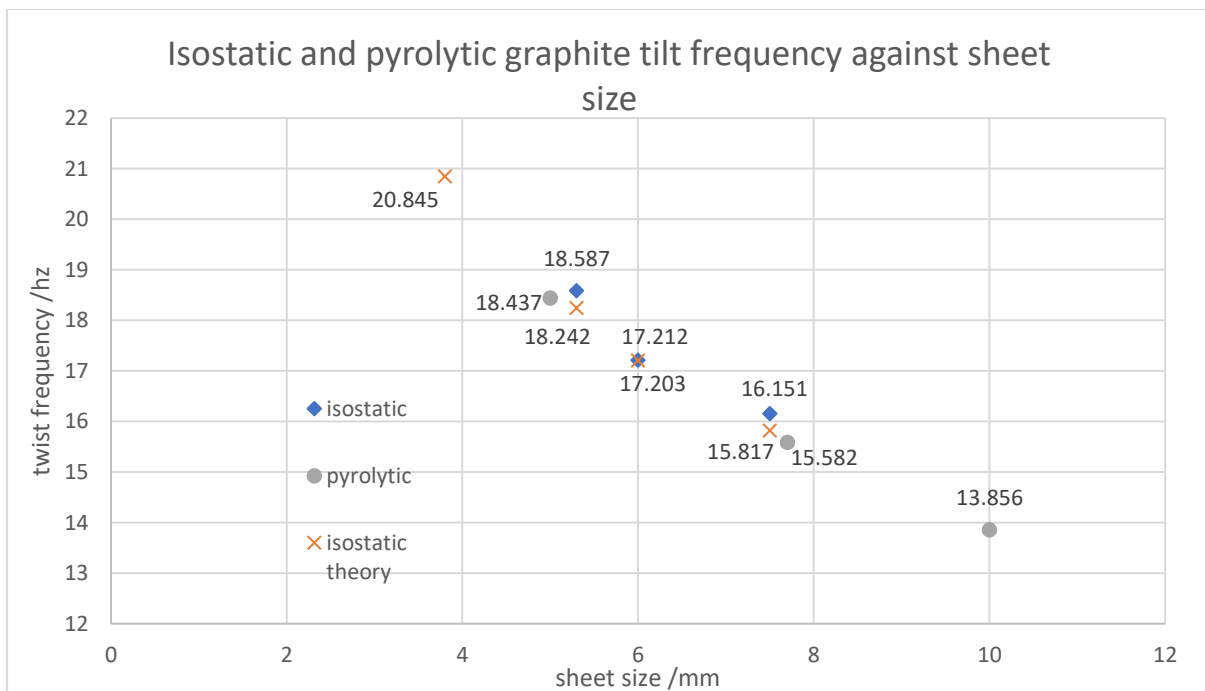


Figure 33 Isostatic and pyrolytic graphite frequencies compared to each other and theoretical values for isostatic